The Atmospheric Oxidizing Capacity in China: Part 1. Roles of different photochemical processes

Jianing Dai[a], Guy P. Brasseur[a,e,f], Mihalis Vrekoussis[b,g,h], Maria Kanakidou [b,d], Kun Qu[b], Yijuan Zhang[b], Hongliang Zhang[c], Tao Wang[f]

[a] Environmental Modelling Group, Max Planck Institute for Meteorology, Hamburg, 20146, Germany
[b] Institute of Environmental Physics (IUP), University of Bremen, Bremen, 28359, Germany
[c] Department of Environmental Science and Engineering, Fudan University, 200433, China
[d] Environmental Chemical Processes Laboratory, Department of Chemistry, University of Crete, Heraklion, 71003, Greece
[e] National Center for Atmospheric Research, Boulder, Colorado, 80307, USA
[f] Department of Civil and Environmental Engineering, The Hong Kong Polytechnic University, Hong Kong, China
[g] Center of Marine Environmental Sciences (MARUM), University of Bremen, Germany
[h] Climate and Atmosphere Research Center (CARE-C), The Cyprus Institute, Nicosia, Cyprus

Correspondence to: Guy P. Brasseur (guy.brasseur@mpimet.mpg.de)

Abstract

The atmospheric oxidation capacity (*AOC*) characterizes the ability of the atmosphere to scavenge air pollutants. However, the processes involved in China, where anthropogenic emissions have changed dramatically in the past decade, are not fully understood. A detailed analysis of different parameters that determine the *AOC* in China is presented on the basis of numerical simulations performed with the regional chemical-meteorological model WRF-Chem. The model shows that the aerosol effects related to extinction and heterogeneous processes produce a decrease in surface ozone of approximately 8-10 ppbv in NO_x-limited rural areas and an increase of 5-10 ppbv in VOC-limited urban areas. In this later case, the ozone increase is noticeable for aerosol concentrations ranging from 20 to 45 µg/m^3 in July 2018. The ozone reduction in NO_x-sensitive regions is due to the combined effect of nitrogen dioxide and peroxy radical uptake on particles and of the light extinction by aerosols, which affects the photodissociation rates. The ozone increase in VOC-sensitive areas is attributed to the uptake of NO_2 by aerosols, which is offset by the reduced ozone formation associated with HO_2 uptake and with aerosol extinction. Our study concludes that more than 90% of the daytime *AOC* is due to the reaction of the hydroxyl radical with VOCs and carbon monoxide. In urban areas, during summertime, the main contributions to daytime *AOC* are the reactions of OH with alkene (30-50%), oxidized volatile organic compounds (OVOCs) (33-45%), and carbon monoxide (20-45%). In rural areas, the largest contribution results from the reaction of OH with alkenes (60%). Nocturnal *AOC* is dominantly attributed to the reactions with the nitrate radical (50-70%). Our results shed light on the contribution of aerosol-related NO_x loss and the high reactivity of alkenes for photochemical pollution. With the reduction of aerosols and anthropogenic ozone precursors, the chemistry of nitrogen and temperature-sensitive VOCs will become increasingly important. More attention needs to be paid to the role of photodegradable OVOCs and nocturnal oxidants in the formation of secondary pollutants.

Keywords: O_3, Atmospheric Oxidation Capacity, Heterogeneous Reactions.

45

50

55

60

65

70

75

80

1. Introduction

With the drastic actions initiated by the Chinese authorities to improve air quality, specifically to reduce the emissions of primary pollutants, including nitrogen oxides (NO_x), volatile organic compounds (VOCs), carbon monoxide (CO), sulfur dioxide (SO_2), and the concentration of particulate matter (PM) suspended in the atmosphere, the level of several secondary pollutants including near-surface ozone (O_3) has increased significantly between years 2013 and 2019, most notably in the North China Plain (e.g., Lu et al., 2018; Liu and Wang, 2020., Wang et al., 2020). Several papers have documented the observed trends of O_3 in China (Lu et al., 2018; Wang et al., 2022). In some cases, studies have provided some explanation for the cause of these trends (Li et al., 2019a., Liu and Wang et al., 2020), specifically in the most polluted areas, or have proposed some mitigation strategies (Li et al., 2019b). Among the formulated hypotheses to explain these trends, the most feasible explanation is the reduction in the level of NO_x in the polluted planetary boundary layer (PBL) with a related reduction in the rate at which O_3 is titrated by nitric oxide (NO) in VOC-limited areas. Another potential cause for the observed O_3 increase is the reduction in the atmospheric aerosol burden and hence in the rate at which peroxy radicals (HO_2 and RO_2) that contribute to O_3 formation are removed by heterogeneous processes (Li et al., 2019a; Liu and Wang, 2020).

Alleviating O_3 pollution requires a quantitative understanding of the different chemical processes that contribute to the photochemical formation and destruction of secondary species. It also requires detailed investigation of the budget of fast-reacting radicals that are directly involved in photochemical oxidation processes. Recent observational studies have documented and analyzed the evolution of several reactive species, such as OH, HO_2 and RO_2 radicals and O_3. On the basis of observations, generally at a single location with routine measurements lasting for several years (Liu et al., 2022, Tan et al., 2019., Zhu et al., 2021., Wang et al., 2022). The sensitivity of ozone, particulate matter and oxidative processes to precursor emissions has also been studied in previous work (Liu et al., 2010; Xing et al., 2017) under highly polluted conditions. Such studies need to be repeated for current conditions characterized by reduced pollutant emissions and aerosol loading.

The purpose of the present study is to provide a quantitative estimate of the different factors that affect the oxidation capacity of the atmosphere in the entire geographical area covered by China. The concept of atmospheric oxidation capacity (*AOC*) has been introduced several decades ago (e.g., Thompson, 1992; Prinn, 2003) to highlight the existence of self-cleansing processes in the atmosphere. These processes allow the removal of most primary pollutants, including methane (CH_4), non-methane hydrocarbons (NMHCs), CO, NO_x, SO_2, as well as the formation of secondary species, including O_3, particulate nitrate (NO_3^-), sulfate (SO_4^{2-}), and secondary organic aerosols (SOA). The oxidation capacity is a measure of the ability of the atmosphere to destroy primary

120   species emitted at the Earth's surface. It is directly linked to the presence of highly reactive radicals, including OH and nitrate radical (NO_3). It is therefore influenced by processes such as photolysis generated by solar radiation, temperature, emission, scavenging processes, atmospheric transport, and other meteorological factors. It is characterized by different factors, including the atmospheric production rate of RO_x radicals (with RO_x defined as $OH + HO_2 + RO_2$, where R

125   represents an organic chain) and the OH reactivity.

    Based on the model simulation, the analysis presented in this paper assesses the relative importance of different photochemical processes that contribute to the formation and destruction of near-surface RO_x and O_3 in different chemical environments encountered in China. This paper is structured

130   as follows. Section 2 first provides some theoretical considerations on which our analysis is based. The adopted regional chemical-meteorological model, described in Sect. 3, is driven by reanalyzed meteorology for the year 2018 and by regional surface emissions that account for the contribution of different sectors. The analysis of the model simulations performed for different conditions is presented in Sect. 4-6. Specifically, the budget of oxidants (RO_x and O_3) is discussed in Sect. 4.

135   The effect of heterogeneous chemical processes in the presence of aerosols is addressed in Sect. 5. Section 6 provides a quantitative estimate of the different indicators that describe the oxidation capacity of the atmosphere. A summary of the principal findings is provided in Sect. 7. Additional information, including the validation of the model simulations, can be found in the Supplementary Information.

140

2. Theoretical considerations

2.1. RO_x radicals

145   As shown in the pioneering paper by Levy (1971), the fate of many primary atmospheric species (CO, CH_4, and NMHCs) and the formation of secondary species, including tropospheric O_3, are associated with cycling chain reactions involving OH, HO_2, and RO_2. In the theoretical description of the key chemical processes presented here, we refer to the simplified reaction scheme listed in Table 1, but the chemical mechanism adopted in our model is considerably more detailed.

150

    The production of RO_x radicals in the troposphere results primarily from the photolysis of O_3 (reactions R1 and R8, see Table 1), of nitrous acid (HONO) (reaction R5), and of different oxygenated volatile organic compounds (OVOCs) such as formaldehyde (HCHO) (reaction R3), larger aldehydes, acetone, etc. (reaction R4). The ozonolysis of alkenes (Alk) (reaction R11) is an additional

155   source of RO_x, which is believed to play a relatively minor role. When considering the sources due to the photolysis of OVOCs, we single out formaldehyde due to the major contribution of this species to RO_x production. OVOCs stand, therefore, for the remaining non-HCHO OVOCs. Thus, we express the production rate of RO_x as

4

160     $P(RO_x) = 2\,k_8\,[O(^1D)]\,[H_2O] + J_{HONO}\,[HONO] + J_{HCHO}[HCHO] + \Sigma_i\,r_i\,J_i\,[OVOC_i]$

    $+ \Sigma_i\,s_i\,k_{11,i}\,[Alk_i]\,[O_3],$

    (1)

Here and in other expressions below, factors k_i represent the reaction coefficients for the reaction
165   i in Table 1, and J is the photolysis frequency for the chemical species under consideration. The
brackets stand for the number densities of species generally expressed in molecules or radicals per
cm^3. Coefficient r_i represents the number of RO$_x$ produced by the photolysis of each OVOCs spe-
cies and s_i is the number of RO$_x$ produced by each alkene ozonolysis reaction. These coefficients
are specific to a reaction involving the photolysis of OVOCs and the ozonolysis of the alkenes. A
170   more explicit form for the two last terms in the above expression depends on the adopted chemical
mechanism. The RO$_x$ source term provides an estimate for the availability of radicals that initialize
photooxidation processes in the troposphere.

The destruction of RO$_x$ radicals results from the termination reactions R15-18 between different
175   RO$_x$ radicals (L_H), reactions R22-24 between RO$_x$ radicals and nitric oxide (L_N) and the heteroge-
neous uptake of HO$_2$ (reaction R28) on aerosol surfaces (L_{het}). Thus, the total destruction rate of
RO$_x$ can be expressed as

    $D(RO_x) = L_H + L_N + L_{het},$
180   (2)

with

    $L_H = \{\,2\,k_{15}\,[OH] + 2\,k_{16}\,[HO_2] + 2\,\Sigma_i\,k_{17}\,[RO_{2,i}]\}\,[HO_2] + 2\,\Sigma_{i,j}\,k_{18,\,i,\,j}\,[RO_{2,i}]\,[RO_{2,j}]$
185

    $L_N = \Sigma_i\,k_{22,\,i}\,[RO_{2,i}]\,[NO] + k_{23}\,[OH]\,[NO_2] + k_{24}\,[OH]\,[NO]$

    $L_{het} = k_{28}\,[HO_2]$

190   In the above expressions, we assume that, near the surface, the RO$_x$ termination reactions between
HO$_2$ and NO$_2$ (that produce nitrous acid, HO$_2$NO$_2$) and between acetyl peroxy radicals and NO$_2$
(that produce peroxyacetyl nitrate, PAN) are balanced by the regeneration of RO$_x$ resulting from
the photolysis of HO$_2$NO$_2$ and the thermal decomposition of PAN (equilibrium conditions), re-
spectively. Therefore, the related reaction rates do not appear explicitly in the above expressions.
195

2.2. Odd Oxygen

In the troposphere, odd oxygen (O$_x$ = O$_3$ + NO$_2$) is produced through complex recurrent radical
reaction chains involving the oxidation of hydrocarbons in the presence of NO$_x$. The O$_3$ molecule

200   is formed by the rapid photolysis of NO_2 (reaction R2) followed by the recombination of atomic oxygen (reaction R7). Reaction R2 is balanced by reactions R19 and R20, which reproduce NO_2. A production of odd oxygen occurs only if NO is converted to NO_2 without consuming O_3, i.e., by reactions R20 and R21 with a peroxy radical (HO_2, CH_3O_2, and other higher-order organic radicals) provided by the oxidation of methane, other hydrocarbons (HC), and by carbon monoxide (reac-

205   tions R9, R10 and R12). The resulting production rate of odd oxygen can be expressed with a good approximation by

$$P(O_x) = k_{20} [HO_2] [NO] + \Sigma_i\, k_{21,i} [RO_2]_i [NO],$$
(3)

210

This equation highlights the nonlinear nature of $P(O_x)$ since the concentration of nitric oxide and peroxy radicals are dependent on each other.

The photochemical destruction of O_x results from several processes, including the photolysis of

215   O_3 (reaction R1) followed by the reaction R8 between the electronically excited oxygen atom $O(^1D)$ and water vapor (H_2O). Other O_x loss mechanisms involve the reactions of ozone with OH (reaction R13), HO_2 (reaction R14), and different alkenes (Alk) (R11). In the presence of NO_x, an additional loss mechanism is provided by the titration of O_3 by NO (R19), followed by the conversion of NO_2 to nitric acid (HNO_3; R23). The total destruction rate of O_x is therefore expressed

220   as

$$D(O_x) = k_8 [O^1D][H_2O] + \{\Sigma_i\, k_{11} [Alk_i] + k_{13} [OH] + k_{14} [HO_2] + k_{19} [NO]\}[O_3] + k_{23}[OH][NO_2],$$
(4)

225   The dominant pathways leading to the formation and destruction rates of O_x and hydroxyl radicals vary according to chemical environments. Under relatively clean conditions with low levels of NO_x, the production of odd oxygen, as provided by reactions R20 and R21, is limited by the availability of NO_x, while the loss of the RO_x radicals is dominated by the peroxy-radical self-reaction R16 that leads to the formation of hydrogen peroxide (H_2O_2) (Song et al., 2021). Under these

230   conditions, a reduction in the emissions of NO_x tends to reduce the ground-level O_3 concentration.

In polluted areas, including many urban centers, the level of NO_x is so high that saturation conditions prevail. In this environment, the formation of O_3 is determined by the availability of VOCs, and the loss of RO_x is dominated by reaction R23 between NO_2 and OH, which produces HNO_3.

235   In this case, a reduction in NO_x tends to increase the concentration of O_3, while a reduction in VOCs is expected to reduce its near-surface abundance (Wang et al., 2022). Furthermore, since highly polluted environments are generally characterized by elevated aerosol loads, the effect of heterogeneous processes on the abundance of reactive species becomes particularly important. Among these reactions, we consider more specifically the uptake of HO_2, NO_2, NO_3, and N_2O_5 on

240   the atmospheric aerosol surfaces (reactions R28-31). The heterogeneous destruction of peroxy radicals on the surface of aerosols tends to inhibit the formation of O_3 by reducing the rate of reactions R20 and R21. Under high levels of aerosols, this reaction may become important for O_3 formation, which has led Ivatt et al. (2022) to define a third O_3 sensitivity regime called the aerosol-inhibited photochemical O_3 regime. The uptake of NO_2 leads to the formation of HONO, whose photolysis

245   represents a significant source of OH. It also forms NO, which reacts with HO_2 and RO_2 to produce O_3. In short, heterogeneous processes may either favor or inhibit the formation of odd oxygen in polluted areas.

The lifetime of O_x in the PBL is sufficiently long (one or two days) that additional processes be-

250   sides photochemical production and destruction need to be taken into consideration. Among them is the additional loss of O_3 and NO_2 resulting from dry deposition on the vegetation. With a deposition velocity of about 1 cm s^{-1} (Wesely et al., 2000), the corresponding odd oxygen loss rate in the boundary layer is close to 1 ppbv h^{-1}, if one assumes that the depth of the mixing layer is in the order of 1 km. In addition, vertical mixing in the convective PBL and advective horizontal

255   transport tend to disperse locally produced O_3 and balance its net production, for example, in urban centers.

2.3. Formulation of aerosol uptake

260   As stated above, heterogeneous chemical reactions can substantially influence the concentrations of RO_x radicals and O_3. The reactions under consideration in our analysis are reactions R28 to R31, listed in Table 1. The first-order reaction rate constant on aerosols k_a [s^{-1}] for species i associated with these reactions is expressed by (Schwartz (1986)):

265    $$k_{a,i} = A_a \left[\frac{a}{D} + \frac{4}{\gamma_{a,i} v_i} \right]^{-1},$$

(5)

where A_a [cm^2 cm^{-3}] is the aerosol surface area density, a [cm] is the mean radius of the particles, D[cm^2 s^{-1}] is the gas-phase diffusion coefficient (Mozurkewich et al., 1987), with the value of

270   0.247 for HO_2 uptake (Xue et al., 2016) and 0.1 for NO_2, NO_3 and N_2O_5 uptake (Gaubert et al., 2020; Liu and Wang., 2020), γ_a is the dimensionless reaction-dependent uptake coefficient for species i, and v_i [cm s^{-1}] is the mean thermal velocity of species i given as a function of temperature T [K] and molecular mass m_i by

275    $$v_i = \left[\frac{8 k_b T}{\pi m_i} \right]^{\frac{1}{2}},$$

(6)

with k_b (1.38 $\times 10^{-23}$ J K^{-1}) being the Boltzmann constant.

280   The chemical substances produced as a result of the HO_2 uptake onto aerosol surfaces are not clearly established and could be H_2O or H_2O_2 (Mao et al., 2010; Mao et al., 2017; Song et al., 2021). Here, to determine the maximum effect of this reaction, we assume that the HO_2 uptake onto aerosols (reaction R28) represents a terminal reaction of the hydrogen radical chain. Hence, water molecules rather than peroxide molecules are assumed to be formed. The corresponding

285   uptake coefficient (γ_{HO2}) is chosen to be 0.1 in this study, a value lower by a factor of 2 than used in some earlier model studies (γ_{HO2} = 0.2; Tie et al., 2001, 2005; Martin et al., 2003; Liu and Wang, 2020; Ivatt et al. 2022), but consistent with the conclusions reached by Gaubert et al. (2020) from their model simulations. These lower values are also adopted by Yang et al. (2022) and are consistent with the measurements of Lakey et al. (2015), Tan et al. (2020), and Song et al. (2020).

290   Specifically, on the basis of observations made in the Beijing-Tianjin-Hebei area during the summer of 2014, Song et al. (2020) conclude that the best fit for the value of γ_{HO2} is a value of 0.116 ± 0.086, which is close to the value adopted in the present study.

The heterogeneous uptake of N_2O_5 by aerosol particles leads to the formation of nitric acid mole-

295   cules (reaction R29). In the present study, we neglect the possible formation of $ClNO_2$ followed by its photolysis into Cl and NO_2. This process associated with the presence of chloride ions in the bulk of the particles is a source of additional radicals and hence could have an influence on O_3 (Thornton et al., 2010; Dai et al., 2020). Here, for the uptake of N_2O_5, we adopt the first-order rate constant as expressed by Bertram et al. (2009) and modified by Yu et al. (2020) with the surface

300   concentrations of the particle chloride and nitrate ions taken from the MOSAIC estimates. This parameterization has been used in simulating the concentration of N_2O_5 in several Chinese sites (Yu et al., 2020), and the simulated levels are in good agreement with the observed N_2O_5 values (Dai et al., 2020).

305   The rate of heterogeneous conversion of NO_3 (reaction R30) is calculated by Eq. (5) with a value of the uptake coefficient equal to 10^{-3} (Jacob, 2000; Xue et al., 2014; Liu and Wang et al., 2020).

Finally, the heterogeneous uptake of NO_2 on aerosol surfaces leads to the production of HONO and HNO_3 (reaction R31), and, as HONO is rapidly photolyzed after sunrise, this heterogeneous

310   process represents a source of OH radicals. The process also converts NO_2 into NO. Here, according to Zhang et al. (2021), we express the first order rate constant by Eq. (5) with a value of the uptake coefficient equal to 8×10^{-6} during nighttime and to $1\times10^{-3} \times (J/J_{max})$ during daytime (Li et al., 2010; Czader et al., 2012; Fu et al., 2019), with J representing the light intensity [W m^{-2}] and J_{max} [W m^{-2}] the peak value of light intensity (chosen to be 400 W m^{-2} in this study).

315

2.4. Other HONO sources

For the particular heterogeneous reaction involving NO_2, which leads to the formation of nitrous acid, we also consider the additional contribution of the uptake on flat surfaces, specifically on
320 bare soils, including asphalt in urban areas. This effect is believed to play a significant role particularly in urban areas (Zhang et al., 2016; Li et al., 2018). Zhang et al. (2021) claim that the measured vertical nighttime profile of this species suggests that the dominant formation nighttime mechanism of HONO results from the heterogeneous conversion of NO_2 on the ground. For this process, which is only crudely represented here, we assume that the first-order rate constant k_g [s^{-1}] for this process is given by Liu et al. (2019) for nighttime conditions
325

$$k_g = \frac{1}{8}\gamma_g v_{NO_2} A_g,$$
(7)

330 where A_g is the surface area density over the bare soil and urban surfaces; γ_g is the uptake coefficient on the ground. Here, according to Zhang et al. (2021), we express a value of the uptake coefficient equal to 4×10^{-6} during nighttime and to $6\times10^{-5}\times(J/J_{max})$ during daytime, where J and J_{max} [W m^{-2}] represent the solar intensity and its maximum value. Following the suggestion of Vogel et al. (2003) adopted, for example, by Zhang et al. (2021), we express the surface density
335 over the ground by $1.7/h$, where h [m] represents the height of the model layer adjacent to the ground; the 1.7 value represents an effective factor per ground surface area in the first layer.

In this model case, we also account for the gas-phase reactions of HONO (R24-R27) as well as the direct transportation HONO emissions. The latter are assumed to be equal to 0.8% of the traffic
340 emission of NO (Dai et al., 2021). In this study, we neglect the direct HONO emissions from soil and the daytime HONO source from the photolysis of NO_3^-, which may lead to an underestimation of HONO concentration in rural areas and during daytime (Zhang et al., 2016, Fu et al., 2021; Zhang et al., 2021).

345 **2.5. Photochemical reactivity and *AOC***

To characterize the oxidation capacity of the atmosphere in China, we consider several indicators that have proven to be useful for developing O_3-controlling strategies. These include the OH reactivity associated with the action of volatile organic compounds (VOC^R) and nitrogen oxides
350 (NO_x^R), the radical chain length (ChL), the ozone production efficiency (OPE), and the atmospheric oxidation capacity (AOC).

Since NO_x, VOCs, and CO are oxidized by the OH radical as part of a cyclic chain process that initiates the O_3 formation, an estimate of the OH reactivity (expressed in s^{-1}) allows us to under-
355 stand the factors that determine the photochemical budget of O_3 and more generally the factors that characterize the atmosphere's oxidizing capacity. The OH reactivity by the different VOCs and CO and by NO_x is defined as

$VOC^R = \Sigma_i\ k_{10,i}\,[\text{VOC}_i] + k_{12}\,[\text{CO}],$

360 (8a)

$NO_x{}^R = k_{23}\,[\text{NO}_2],$

(8b)

365 The radical chain length *ChL* provides a measure of the number of cycles affecting RO_x radicals before these radicals undergo a termination process. It can therefore be expressed by the ratio between the conversion rate between RO_x radicals, including the conversion by NO of HO_2 to OH (reaction R20) and of RO_2 to HO_2 (reaction R21), and the destruction rate of RO_x (or equivalently by the production rate of RO_x). Thus, adopting here the definition of Martinez et al. (2003), Mao

370 et al. (2010), and Zhu et al. (2020), we write

$$ChL = \frac{k_{20}[HO_2][NO] + \Sigma_i k_{21,i}[RO_{2,i}][NO]}{D(RO_x)},$$

(9)

375 From this adopted definition Eq. (9), and assuming that the RO_x production and destruction rates are in balance, we can write

$$P(O_x) \cong P(RO_x)ChL,$$

(10)

380

which shows that O_x production is proportional to the RO_x production rate and is favored by a large number of radical regenerations.

The Ozone Production Efficiency (*OPE*) is used to quantify the efficiency of O_3 molecules formed

385 per NO_x molecule oxidized. It is defined as the ratio between the O_3 production rate and NO_x loss rate

$$OPE = \frac{P(O_x)}{D(NO_x)} \cong \frac{P(O_x)}{P(HNO_3)},$$

(11)

390

and represents the efficiency of NO_x. To a good approximation, this expression can be expressed as

$$OPE \approx \frac{k_{20}[HO_2][NO]}{k_{23}[OH][NO_2]},$$

395 (12)

As the instantaneous value of *OPE* depends on the HO$_2$/OH and NO/NO$_2$ concentration ratios, it accounts for the couplings between RO$_x$ and NO$_x$ cycles. One can show that this factor is usually highest in the remote atmosphere or low-NO$_x$ environments (Ridley, 1999). Note that, under VOC-limited conditions (polluted areas) when the production rate of odd oxygen can be expressed as (Kleinman et al., 2002)

$$P(O_x) = \sum_i \varphi_i \, [VOC_i][OH],$$
(13)

where φ_i represents the O$_3$ yield from the production of HO$_2$ radicals, *OPE* can be approximated by

$$OPE \approx \overline{\varphi} \frac{VOC^R}{NO_x^R},$$
(14)

where $\overline{\varphi}$ represents an average yield value. In other words, under VOC-limited situations, the ratio between VOC^R and NO_x^R has some similarities with the odd oxygen production efficiency.

Finally, the atmospheric oxidizing capacity (*AOC*; expressed in cm^{-3} s^{-1}), a parameter introduced by Geyer et al. (2001) to account for the contribution of all oxidants, is derived here as the rate at which CO, CH$_4$, and NMHCs (all species are noted here as Y_i) are oxidized by OH, O$_3$, and NO$_3$ (noted as X_j) (Geyer et al., 2001; Elshorbany et al., 2009; Xue et al., 2016; Wang et al., 2022; Yang et al., 2022). Thus, when considering all combinations of the different primary pollutants and atmospheric oxidants, we write

$$AOC = \sum_i^j k_{i,j} \, [Y_i][X_j],$$
(15)

As stated by Wang et al. (2022) and Yang et al. (2022), *AOC* is a parameter well-suited to describe the removal rate of primary pollutants and the formation of secondary species including O$_3$ and secondary PM$_{2.5}$. It is, therefore, an indicator used to design control policies for these secondary species. During daytime, the largest contribution to *AOC* is due to the oxidation of pollutants by the OH radical (Li et al., 2017; Liu et a., 2022). At night, the oxidizing capacity is due to the oxidation by NO$_3$ and O$_3$ (Brown and Stutz , 2012, Ng et al., 2017).

3. Model description and validation

3.1. Modeling setting

To characterize the chemical budget of reactive species, photochemical parameters and *AOC* in China, we use the version 4.1.2 of the WRF-Chem model (Skamarock et al., 2019) to simulate the meteorological fields as well as the regional transport, the chemical and physical transformations of trace gases and aerosols. We adopt the MOZART-4 gas-phase chemical mechanism documented and evaluated by Emmons et al. (2010), which includes 108 chemical species and 235 gas-phase reactions. This scheme is coupled to the MOSAIC aerosol module described by Fast et al. (2006), Zaveri et al. (2008), and Lu et al. (2021). A list of detailed RO_2, VOCs and aerosol species included in the model is provided in Table S1 in the Supplementary information.

We select one month in the winter (1st to 31st January) and the summer (1st to 31st July) of 2018 respectively to analyze the calculated distributions of chemical species. The horizontal resolution adopted in the present study is 36 km × 36 km over the entire domain that covers East and Southeast Asia (from 15° S to 60° N in latitude and 60° E to 150° E in longitude). Initial meteorological conditions are taken from the NCEP reanalysis dataset FNL (http://rda.ucar.edu/datasets/ds083.2/). Initially chemical boundary conditions are constrained by the results of the global CAM-chem model (https://www.acom.ucar.edu/cam-chem/). The different modules used to represent physical processes are provided in Table S2.

For the anthropogenic emissions of air pollutants, we adopt the surface emissions provided by the Multi-resolution Emission Inventory for China (MEIC v1.3; http://www.meicmodel.org/) derived for the year 2017 (Zhang et a., 2009; Zheng et al., 2018). This inventory covers the anthropogenic emissions for the geographical area of mainland China. For the remaining areas of Asia, we use the anthropogenic emissions provided by the 2018 global inventory of the Copernicus Atmosphere Monitoring Service (CAMS)-GLOB-ANT_v4.2 (Elguindi et al., 2020; Granier et al., 2019). Biogenic emissions are calculated online by the Model of Emission of Gas and Aerosols from Nature (MEGAN) version 2.1 (Guenther et al., 2006). The dust and sea-salt emissions are calculated online by the Global Ozone Chemistry Aerosol Radiation and Transport (GOCART) module (Chin et al., 2002).

The availability of several observational datasets allows us to evaluate the meteorological parameters and air pollutant concentrations derived by our regional model. The meteorological data used to validate the model simulations, including the wind direction, wind speed, surface temperatures, and specific humidity, are obtained from the NOAA National Climatic Data Center (NCDC). Conventional air pollutant data, including SO_2, NO_2, CO, O_3, and $PM_{2.5}$, are obtained from the surface stations of China's Ministry of Ecology and Environment (MEE; https://www.mee.gov.cn/). To validate the model results, we calculate the mean bias, the normalized mean bias, the normalized mean error, the root mean square errors, and the correlation coefficient (See Table S3). The equations for these statistical parameters are found in the paper by Dai et al. (2020).

475 In our analysis presented in the subsequent sections, we examine in more detail the calculated concentrations of photochemical parameters at urban sites in four large cities in China: Beijing, Shanghai, Guangzhou, and Chengdu (Fig. 1). We also provide these parameters at four rural observational sites for which detailed observational analysis is available. These include the relatively polluted site of Wangdu in the suburban region near Beijing, the Atmospheric Supersite of Heshan

480 located 50 km to the southwest of Guangzhou, the remote free site of Waliguan at about 3800 m altitude, and the coastal site of Hok Tsui in Hong Kong. Detailed information on the selected sites in the present study is listed in Table 2.

3.2. Design of numerical experiments

485

Table 3 lists the different sensitivity cases designed for this study. The baseline case, called *Het-all*, accounts for all heterogeneous reactions referred to in Table 1 and includes all identified sources of HONO mentioned in Sect. 2.4. The *Het-all* case is used to evaluate the performance of the model relative to observations. To quantify the specific aerosol effects through the uptake of

490 HO_2, N_2O_5, NO_3 and NO_2 and extinction, and NO_2 uptake over the ground on surface O_3 concentration, other nine sensitivity cases are considered based on different assumptions. The details on these sensitivity cases are given as follows.

For the specific effects of aerosol uptake, the respective importance of these processes is deter-

495 mined by subtracting the baseline results from the results in sensitivity cases in which specific heterogeneous reactions are ignored: HO_2 (*No-HetHO2-Aero*), NO_3 (*No-HetNO3-Aero*), N_2O_5 (*No-HetN2O5-Aero*), NO_2 (*No-HetNO2-Aero*). The case labeled *No-Het-Aero* ignores all the above heterogeneous reactions on aerosols. The difference between *Het-All* and *No-Het-Aero* represents the combined effects of these heterogeneous reactions on particles. The case denoted as

500 *No-Phot* ignores the radiative effects of aerosols on the calculation of the photodissociation coefficients. The difference between *Het-All* and *No-Phot* represents the effect of aerosol radiation. An additional case labeled as *No-Het-Aero-Phot* ignores the above-mentioned heterogeneous reactions on aerosols and aerosol effects on light extinction and photodissociation to quantify the combined effect of aerosol uptake and radiation.

505

In order to quantify the contribution of HONO sources added to the model, we consider a case labeled *No-HONO* in which the heterogeneous uptake of NO_2 by aerosols, bare soils, urban surfaces as well as the homogeneous formation, and surface emissions of HONO are all ignored. The difference between the results of the *Het-All* case and the *No-HONO* case represents the effect of

510 all HONO sources. The final case, denoted as *No-Het-HONO-Phot,* ignores all the above heterogeneous reactions on aerosols, other HONO sources, and the radiative effects of aerosols on the calculation of the photodissociation coefficients. The difference between *Het-All* and *No-Het-HONO-Phot* provides quantitative measures of the effects resulting from all heterogeneous reactions (aerosols and ground effects), other HONO sources, and aerosol radiation.

3.3. Model validation

In Figure S1, we compare the spatial distribution of the calculated surface concentrations of the Maximum Daily 8-hour average (MDA8) O_3, as well as the monthly averages NO_2, CO, and $PM_{2.5}$
520 (*Het-all* case) with available observational data from MEE for January and July 2018. In most cases, this comparison shows a good performance of the model with, however, some discrepancies: an overestimation of summertime O_3 in central and western China associated with an underestimation of NO_2 in these regions, an underestimation of summertime O_3 in eastern China with a slight overestimation of NO_2 (Fig. S1). In the case of CO and $PM_{2.5}$, the calculated concentrations
525 are higher than the measured values in central China in both seasons.

One should stress here that a comparison of coarse resolution model output with local measurements made at ground stations is not straightforward and can only provide crude information. In order to alleviate the problem, we have combined the concentration values measured by different
530 stations within a given area with the 36 km resolution model results. The areas including the individual stations in metropolitan areas are provided in Table 2.

The diurnal variation of NO_2, O_3, CO, and $PM_{2.5}$ in January and July for the four metropolitan areas selected in our study are compared with measurements from monitoring stations in Fig. S2
535 and S3. The model successfully simulates the diurnal variations of these chemicals. However, the summertime NO_2 concentration is overestimated in these urban areas. Summertime ozone concentrations are underestimated at night and overestimated during daytime. These discrepancies can be explained by the relatively lower NO_2 uptake coefficients used in our studies (Liu et a., 2019; Fu et al., 2019) and the coarse resolution of the model (Tie et al., 2010). An overestimation of the
540 NO_2 concentration tends to broaden the area in which ozone is VOC-controlled.

The simulated CO concentration is slightly overestimated, which can be attributed to uncertainties in chemical boundary conditions and in the emissions (Liu and Wang et al., 2020). An overestimation of $PM_{2.5}$ is found in summer, which can be partially due to uncertainties in emissions and
545 the mechanisms of secondary aerosol formation (Li et al., 2022). Model estimates of the NO, HONO, HCHO, OH, HO_2, NO_3, isoprene, ethane, and ethene mixing ratios for the base case are found in Fig. S4-S6. Calculated diurnal variations of surface NO, HONO, OH, HO_2, and NO_3 are provided in Fig. S7-S11. Generally, based on the comparison of our simulated results with observed data in the literature, our simulated concentrations of OH, HO_2, HONO, and HCHO match
550 relatively well with the observational data. The calculated aerosol surface area density is shown in Fig. S12. The values calculated in eastern China are considerably higher during wintertime (2.5 to 3×10^{-5} cm^2 cm^{-3}) than during the summer (0.7 to 1.0×10^{-5} cm^2 cm^{-3}).

The validation of the model regarding volatile organic compounds is not easy to perform because of the short lifetime of most of these species, the inhomogeneity in their emissions, the complexity of the chemical processes involved, and the lack of observational data. In China, only a few stations report continuous measurements of VOCs. The comparison is made particularly difficult with a model whose grid size is equal to 36 km. Therefore, as an illustrative example, we show in Fig. S13 of the Supplementary material, a comparison of the calculated and observed diurnal variation in the mixing ratio of ethane, propene, isoprene, ethane, propane, benzene, toluene, and xylene at the Hok Tsui site (Hong Kong) in January 2018. The discrepancies in the calculated concentrations of anthropogenic VOCs and of biogenic isoprene lead to inaccuracies in the calculated concentrations of secondary organic species such as formaldehyde as well as in the calculation of the OH reactivity (VOC^R) and of the atmospheric oxidation capacity (AOC).

More detailed information on the model validation is provided in the Supplementary Information.

4. The budget of oxidants

In order to highlight the regional differences in the existing photochemical regimes, we first show the distributions of the areas where the ozone formation is either NOx- or VOC-limited. As an indicator to define these areas, we adopt the ratio between the H_2O_2 to HNO_3 production rate. An area is considered to be NOx-limited if this ratio is larger than 0.2 and VOC-limited if it is less than 0.06 (Zhang et al., 2009).

Figure 2 shows that, during summertime, the ozone formation rate is primarily sensitive to NOx in southern and western China as well as in the surrounding oceanic regions. Exceptions are found at the south-eastern coast, which is strongly influenced by the metropolitan regions of Guangzhou and Hong Kong. During this season, the formation of ozone is VOC-sensitive in a large fraction of northern China, specifically in the areas to the south of Beijing and in the vicinity of Shanghai. A broader area surrounding Beijing and Shanghai corresponds an intermediate situation (transition). A similar situation prevails in and around urban hotspots such as Seoul and Tokyo. During winter, the ozone formation in most of eastern and northern China is VOC-limited

4.1. The budget of RO$_x$

Figure 3 shows the geographical distribution of the average daytime (08:00-19:00 Local Standard Time) production rate of RO$_x$ ($P(RO_x)$) contributed by the photolysis of HONO, HCHO, non-HCHO OVOCs and O_3 for the January and July of 2018.

In winter, the mean daytime production rate of the radicals is small in less populated western China. In the eastern plain, its value associated with the HONO photolysis is typically 0.5-0.8 ppbv h^{-1} in rural areas and reaches 1-2 ppbv h^{-1} in polluted urban areas. The contribution of the HCHO photolysis to $P(RO_x)$ is of the order of 0.15 ppbv h^{-1} in most areas, with values as high as 0.5 ppbv

h^{-1} in Guangzhou, which benefits from sufficient solar radiation during winter. Correspondingly, the contribution of other OVOCs is around 0.2 ppbv h^{-1} in southern China, with a similar distribution of the photolysis of HCHO. The mean daytime $P(RO_x)$ associated with O$_3$ photolysis is small (less than 0.5 ppbv h^{-1}) over the entire Chinese territory except in the very south of the country, where it reaches 0.2 ppbv h^{-1}. The contribution by alkene ozonolysis is negligible (Fig. S14).

In summer, the mean $P(RO_x)$ by HONO photolysis reaches 2 to 3 ppbv h^{-1} in the regions surrounding Beijing, Shanghai, Guangzhou, and Chengdu but is considerably smaller (less than 0.5 ppbv h^{-1}) in the outskirt rural areas. The photolysis of HCHO reaches values ranging from 0.5 to 1.0 ppbv h^{-1} in the rural areas of eastern China, with no particular maximum in metropolitan areas. The high value of $P(RO_x)$ contributed by non-HCHO OVOCs photolysis, ranging from 0.3 to 0.8 ppbv h^{-1}, with obvious peak values in city areas. The daytime averaged value of $P(RO_x)$ resulting from the photolysis of O$_3$ is of the order of 1.0 ppbv h^{-1} in eastern and southern China. The peak spot in the Sichuan basin is due to the high water vapor contributed by heavy rainfall in summer, which leads to high OH radical (Xia et al., 2021).

In summary, and for the present conditions, our model suggests a higher value of $P(RO_x)$ in summer than in winter. The higher summertime $P(RO_x)$ in eastern and southern China is associated with the photolysis of formaldehyde and O$_3$. In urban areas, the dominant contribution to the higher $P(RO_x)$ in summer is provided by the photolysis of HONO. The spatial distributions that vary in winter and summer are also related to the seasonal variations in meteorological parameters, such as surface temperature and water vapor (Fig. S15).

The diurnal variation of the $P(RO_x)$ in four different metropolitan areas (Beijing, Shanghai, Guangzhou, and Chengdu) at two relatively polluted rural (Wangdu and Heshan) and two clean remote sites (Hok Tsui and Waliguan) is shown for summertime in Fig. 4. The graph shows the contribution of the HONO (green area), HCHO (red area), non-HCHO OVOCs (dark green area), and O$_3$ (yellow green area) photolysis, as well as the effect of alkene ozonolysis (blue area). In the four urban centers, the maximum values of $P(RO_x)$ in the early afternoon range between 5 ppbv h^{-1} in Shanghai and 6-8 ppbv h^{-1} in the three other cities. In the early morning, as the sun rises, the largest contribution is due to the photolysis of HONO. A few hours later, the contribution of the photolysis of HCHO and other OVOCs becomes large. The value of $P(RO_x)$ from the photolysis of O$_3$ is small in the early morning and peaks in the mid-afternoon. In the four sites of the rural areas, the maximum value of $P(RO_x)$ is close to 5 ppbv h^{-1} in Wangdu (suburban site southwest of Beijing), 1.3 ppbv h^{-1} in Heshan (rural site close to Guangzhou), and less than 0.3 ppbv h^{-1} in Hok Tsui (coastal site) and Waliguan (western China). The contribution of O$_3$ photolysis generally dominates at these rural sites.

A comparison between the values of $P(RO_x)$ derived from local observations is performed with model estimates in Table 4. At four city sites, our simulated values of the maximum of $P(RO_x)$

16

and the contribution by the photolysis of HONO, HCHO and O_3 reproduce satisfactorily the observations. However, at the Heshan site, the calculated value of $P(RO_x)$ (1.1 ppbv h^{-1}) in our study is much smaller than the observed value (4.0 ppbv h^{-1}) (Tan et al., 2019). One reason for this discrepancy may be the missing soil HONO emission, which leads to an underestimation of HONO concentration at this site (Table S4) and the contributed value to $P(RO_x)$ by the photolysis of HONO (0.5 ppbv h^{-1} v.s. 2.0 ppbv h^{-1}). Another uncertainty is the contribution of non-HCHO OVOCs photolysis to the $P(RO_x)$. Wang W. et al. (2022), based on the measurement data in Guangzhou, reported that a model without constraints of non-HCHO OVOCs would lead to an underestimation in the production rate of RO_x and O_3. Owing to the lack of specific OVOCs measurements, it is difficult to quantify the contributions of different OVOC species. Additional efforts regarding the OVOC measurements are needed to understand the specific contribution of OVOCs to the atmospheric oxidation capacity.

The diurnal variations of $P(RO_x)$ are displayed in Fig. S16. The maximum value of the $P(RO_x)$ is close to 3 ppbv h^{-1} in Beijing, Chengdu and Shanghai and is about twice as large in the region of Guangzhou. In Wangdu and Heshan, the peak values are comparable to those in urban areas, while in Hok Tsui and Waligan, they are lower than 1 and 0.1 ppbv h^{-1}, respectively. In most cases, the major contribution to $P(RO_x)$ is provided by the photolysis of HONO.

The spatial distribution of the daytime averaged destruction rate for RO_x ($D(RO_x)$) in January and July is shown in Fig. 5. In the two seasons under consideration, the loss rate is the largest in the eastern and southern regions of China. In January, this quantity is largest in polluted metropolitan areas, with daytime mean values surpassing 2 ppbv h^{-1}. In July, the total daytime average value of $D(RO_x)$ is of the order of 3 ppbv h^{-1} in the rural areas of eastern China and reaches about 6 ppbv h^{-1} in the urban and industrialized areas. In Tibet, the value of this quantity is small (~0.1 ppbv h^{-1} in winter and 1.2 ppbv h^{-1} in summer).

Interestingly, the relative importance of the different photochemical mechanisms involved in the destruction rate $D(RO_x)$ varies considerably with the season. In January, the $D(RO_x)$ due to the reaction between OH radicals and NO_x (L_N in Eq. 2) dominates in most parts of eastern China (contribution of typically 90%) except in Tibet, where the largest loss (contribution of 70-80%) is due to the recombination of hydrogen radicals (L_H in Eq. 2). In July, it is this last type of loss (L_H) that plays the dominant role (typically 90%), except in the eastern plain of China where the level of NO_x is highest, and L_N (contribution of 70-80%) is, therefore, larger than L_H (contribution of 20%). In both seasons, the destruction of RO_x by the uptake of HO_2 is relatively small (generally less than 15%). The highest contribution occurs during winter in southwestern China (contribution of 30%) and in the Ganges River Valley of India (contribution of 40%).

The diurnal variation of $D(RO_x)$ in July is presented in Fig. 6 in four urban areas (Beijing, Shanghai, Guangzhou, and Chengdu) and in four selected locations in rural areas (Wangdu, Heshan,

Hoktsui, and Waliguan, see Fig. 1). In the summertime, the value of $D(RO_x)$ around noon reaches about 13 ppbv h^{-1} in the urban areas except in Shanghai, where it reaches only 8 ppbv h^{-1}. In winter, the corresponding maximum values are closer to 3-4 ppbv h^{-1}, except in the southern city of Guangzhou, where the maximum loss rate is closer to 6 ppbv h^{-1}. In all these cases, the dominant contribution to $D(RO_x)$ is attributed to the reactions involving the presence of NO_x (L_N). In rural areas, the value of $D(RO_x)$ is considerably smaller. In July, it is of the order or smaller than 2 ppbv h^{-1} and is dominated by the HO_x recombination (L_H). In the wintertime, the peak loss is smaller than 0.2 ppbv h^{-1} except in Chengdu, where it reaches 0.4 ppbv h^{-1}. The major contribution is due to the reactions involving NO_x (L_N).

The experimental study of Whalley et al. (2021) in Beijing during the summer of 2018 provides for $D(RO_x)$ a maximum daytime value of 7 ppbv h^{-1} with the following contributions: 4 ppbv h^{-1}, 1.3 ppbv h^{-1}, and 1 ppbv h^{-1} for the $NO_2 + OH$, $NO + OH$, and $RO_2 + OH$ reactions, respectively. Our simulated value matches well the reported experimental data, and the corresponding values in July are 5 ppbv h^{-1}, 0.8 ppbv h^{-1}, and 1.2 ppbv h^{-1}, respectively. Yang et al. (2021) report diurnal variations in $D(RO_x)$ as derived from their observation in Chengdu during the autumn of 2018. The peak value of this quantity is about 7 ppbv h^{-1}, which is lower than our calculated value of 12.5 ppbv h^{-1} in July. The higher level in our study is due to the overestimated concentration of summertime NO_2 in Chengdu (Fig. S2). This overestimation also leads to a higher contribution of the $NO_2 + OH$ reaction by 55% in our study than the reported 35% in the literature. The calculated values of $D(RO_x)$ depend on the concentration values of the NO_x and HO_x radicals as provided by the model with the related uncertainties. The model overestimation of NO_2 reported in Section 3.3 (Fig. S2) may lead to an quantitative error in the relative contributions of the different radicals to $D(RO_x)$ in other city sites (Guangzhou city).

4.2. The budget of odd oxygen

The production rate of odd oxygen ($P(O_x)$) with its two contributions (reaction of NO with hydrogenated and organic peroxy radicals (HO_2 and RO_2) shown in Eq. 3) is shown in Fig. 7 for January and July 2018. In the Northern China Plain and other urbanized areas, the production rate is of the order of 4-6 ppbv h^{-1} during winter (January), while in the rural areas of southern China, it is larger than 20 ppbv h^{-1} during summer (July) and 6-10 ppbv h^{-1} during winter. The value of $P(O_x)$ is very small in the western part of China. The relative contributions of both step-limiting processes to the total $P(O_x)$ are of the same order of magnitude, although the reaction involving the hydrogenated peroxy radicals seems to slightly dominate, particularly outside densely populated areas.

The diurnal variations in $P(O_x)$ are depicted in Fig. 8 for specific areas of China in July. This graph highlights the maximum values found during the early afternoon in urban areas: 115 pphv h^{-1} in Beijing, 40 pphv h^{-1} in Shanghai, 110 ppbv h^{-1} in Guangzhou, and 70 ppbv h^{-1} in Chengdu. In Beijing, Whalley et al. (2021) derived from their observations in the summer of 2018 a maximum

O_x production rate of 100 ppbv h^{-1}. These high values must be contrasted by the considerably lower values found in rural areas: 1.5 ppbv h^{-1} at Mount Walinguan and Hok Tsui. Intermediate maximum values are found at the sites located in the vicinity of large metropolitan areas: 40 ppbv h^{-1} in Wangdu and only 7 ppbv h^{-1} in Heshan. The graph also shows the relative contribution of the hydrogen and organic peroxy radicals. Both radicals contribute about equally to the odd oxygen production rate. The contribution of the organic peroxy radical is determined by anthropogenic emissions of hydrocarbons in the cities and by biogenic hydrocarbons in rural areas. A similar representation of the factors contributing to the formation of O_x during winter is shown in Fig. S17.

Finally, a quantitative estimate of Eq. (4) is provided in Fig. 9. In the eastern regions of China, the largest contribution to the diurnal mean value of $D(O_x)$ is due to the reaction between NO_2 and OH, particularly in winter. This chemical path remains, however, the dominant loss channel during summer in the polluted northern plain between Shanghai and Beijing. In urbanized area, the reaction between H_2O and $O(^1D)$ also play a relatively considerable role on the value of $D(O_x)$ in summer. The relative contribution of ozonolysis reaction with alkene to the value of $D(O_x)$ is displayed in the southern China, which is associated with the high level of alkene in this area. In rural areas, the highest contribution is from the reaction between H_2O and $O(^1D)$ in summer, followed by the reaction between HO_2 and O_3.

5. Effects of aerosols on oxidants

The presence of aerosols in the atmosphere affects the abundance of atmospheric oxidants primarily through two different processes: (1) changes in the heterogeneous reaction rates associated with the uptake of several species by the particles (Tan et al., 2020; 2022), and (2) changes in the photolysis rate associated with enhanced extinction of solar light (Tie et al., 2001; 2005; Xing et al., 2017; Tan et al., 2022). Here we assess the relative importance of these two different mechanisms and derive the combined effect on the concentration of surface O_3.

5.1. Effects due to heterogeneous reactions

Figure S18 summarizes the response of surface NO, NO_2, OH, and HO_2 concentrations to the introduction of the added heterogeneous chemical reactions (R28-31 in Table 1) in the model. The concentration of NO_x species decreases due to the enhanced conversion of NO_x into HNO_3. In the eastern plain of China, we derive a reduction of up to 9 ppbv for NO_2 and 3 ppbv for NO in winter, with a summertime decrease of 6 ppbv for NO_2 and 2 ppbv for NO. At the same time, the concentration of HO_x increases due to the enhanced formation of HONO, which is a source of HO_x in the presence of sunlight. This process overrides the expected reduction in HO_2 due to its uptake by the aerosol. We find an increase of up to 0.15 pptv for OH and 5 pptv for HO_2 in winter, and 0.3 pptv for OH and 8 pptv for HO_2 in summer.

We now examine how the uptake of HO_2, N_2O_5, and NO_2 on the surface of particles modifies the surface concentration of near-ground O_3 (Fig. 10). As shown by Fig. 10a, the uptake of HO_2 onto aerosols in January leads to a reduction in the surface concentration of ozone of about 3-4 ppbv, with a large decrease concentrated in Sichuan Basin and central China. In July (Fig. 10b), the highest ozone changes are found in the North China Plain, especially in the vicinity of Beijing (about 3 ppbv). The high spots of aerosols effect of HO_2 uptake on ozone are associated with the spatial distribution of the aerosol surface area density. In winter (Fig. S12), high values of aerosol surface area density are derived in Sichuan Basin and central China, while, in summer, high values are calculated in Beijing and surrounding areas. The high sensitivity of the HO_2 uptake on particles to the aerosol geometric parameters has been highlighted by Song et al., 2020. Finally, we assess how the assumption made on the product of the HO_2 uptake influences our model results. Figure S21 in the Supplementary Information shows the differences in calculated near-ground mixing rations of OH, HO_2, H_2O_2, and ozone when the heterogenous conversion of HO_2 is assumed to produce hydrogen peroxide rather than water molecules.

The response of ozone to the uptake of N_2O_5 by aerosols is negative during winter when the competing photochemical conversion of NO_x to HNO_3 by the OH radical is very slow. The heterogeneous conversion of N_2O_5 to HNO_3 tends to reduce ozone by up to 3-4 ppbv in southern China during winter (Fig. 10c), with limited effects in the summertime (Fig. 10d).

The uptake of NO_2 by aerosols tends to increase the wintertime ozone concentration by 8-9 ppbv in eastern China and in large urban areas of southern China (Fig. 10e) since the photolysis of HONO (formed from the heterogeneous NO_2 conversion) leads to enhanced concentrations of NO and OH. As the simulated value of wintertime HO_2 is low (below 0.5 pptv) in large parts of China, the production of HO_x, from the photolysis of HONO, dominantly controls the value of $P(RO_x)$ (Fig. S14) and the formation of O_3 in this season. In summer (Fig. 10f), the concentration of ozone is reduced by 3-6 ppbv in the NO_x-sensitive rural areas of eastern and central China but is enhanced by 6-7 ppbv in VOC-sensitive urban areas. During this season, the high value of the HO_2 density weakens the contribution of the HO_x produced by the HONO photolysis. However, the lower level of summertime NO_x strengthens the effect of the NO_2 loss resulting from the NO_2 uptake on particles.

The effect on near-surface ozone of the heterogeneous conversion of NO_3 by aerosols, also considered in the present model study (not shown), has been found to be very small.

The lowest panels of Fig. 10 show the change in ozone resulting from all four heterogeneous processes on aerosol surfaces. When combining the effects of all HO_2, NO_2, NO_3, and N_2O_5 heterogeneous reactions, we derive an ozone increase of 6-8 ppbv in winter and a decrease of 6-8 ppbv

in summer. However, ozone increases up to 8 ppbv in the VOC-limited metropolitan areas of Beijing, Shanghai, Guangzhou, and Chengdu. Comparison of Fig. 10 e, f with Fig. 10 g, h, respectively, suggests that heterogeneous loss of NO_2 on atmospheric particles discussed above dominates the impact of the studied heterogeneous reactions on surface O_3.

The O_3 response to the uptake of HO_2 and NO_2 is complex. The $HO_2 + O_3$ reaction provides a direct destruction mechanism for ozone, and the heterogeneous uptake of HO_2 contributes, therefore, to ozone enhancement. At the same time, the HO_2 uptake reduces the ozone production resulting from the reaction between HO_2 and NO, a photochemical process that is most efficient during summertime. The conversion of NO_2 to HNO_3 tends to reduce the O_3 formation in NO_x-limited areas due to the loss of NO_2 by particles. However, in VOC-limited areas, the loss of NO_2 leads to an increase in the O_3 concentration. Moreover, the photolysis of HONO, which results from NO_2 uptake, produces NO and OH, which further affects the formation of O_3.

Our model simulation in July suggests that the presence of aerosol leads to a decrease of O_3 in NO_x-limited areas and an increase of O_3 in VOC-limited areas. In other words, the continuous reduction in aerosol emissions observed in the past years should have led to an increased ozone concentration in NO_x-limited areas and a reduced ozone concentration in VOC-limited areas. The O_3 decrease in VOC-limited areas is the result of two opposite effects: the ozone decrease due to reduced NO_2 uptake (increased NO_x densities and enhanced ozone titration), and the ozone increase from reduced HO_2 uptake (increased HO_2 concentration and enhanced rate of the $HO_2 +$ NO reaction). The importance of HO_2 uptake by aerosols on ozone formation has been highlighted by several modeling studies (Li et al., 2021; Liu and Wang, 2021; Ivatt et al., 2022). However, recent studies based on field measurements (Tan et al., 2020; 2022; Dyson et al., 2022; Yang et al., 2021) made in the urban/rural areas of northern and southern China (Wangdu, Beijing, Shenzhen, and Chengdu) during the summertime of 2014, 2017, 2018, and 2019, highlighted the minor importance of HO_2 uptake for radical chemistry and O_3 formation, and showed the increasing importance for the ozone production of the reduced NO_2 uptake by particles. One potential reason for changes in the conclusions of these studies could be attributed to the sharp reduction in the emissions of pollutants in China (Zheng et al., 2018), including the reduction in the aerosol load and in the anthropogenic NO_x emissions. Another possible explanation is the adoption for the analyses of different values for the uptake coefficients and for the aerosol geometric parameters associated with the heterogeneous reactions affecting NO_2 and HO_2.

5.2. Effects due to photolysis

The presence of aerosols in the atmosphere tends to enhance the absorption and scattering of incoming solar radiation with direct impacts on the photolysis rates and hence on the abundance of chemical species. Figure S19 shows a model estimate of the resulting effects on the surface concentrations of NO_2, NO, OH, and HO_2.

In the month of January, during which the aerosol burden is high, and the solar intensity is low, the effect of light reduction by the aerosols through changes in the photolysis rates tends to increase the surface concentration of NO_x, especially in the most populated and polluted urban areas (Beijing, Shanghai, and Chengdu) where an increase in the concentration of NO_2 typically 0.5 ppbv is derived. In these urban areas, the concentration of NO is increased by 0.5 ppbv. A reduction in surface OH (about 0.1 pptv) and HO_2 concentrations (about 1.5 pptv) is derived, with the largest effect occurring in the southeastern regions of China. The surface O_3 decreases by up to 4-5 ppbv (Fig. 11a), with the highest decrease found in the Sichuan basin. In July, the aerosol burden is lower, while the solar intensity is higher. The effect of light reduction by the aerosols tends to increase the surface concentration of NO_2 by 1 ppbv in the North China Plain. In the case of OH and HO_2, a decrease of 0.05-0.1 pptv and 2-3 pptv is found in the North China Plain. A decrease of O_3 by up to 3-4 ppbv is derived in the Beijing and surrounding area (Fig. 11b).

5.3. Combined aerosol effects on ozone (uptake effects and photolysis).

When all heterogeneous processes affecting HO_2, N_2O_5, and NO_2 are simultaneously taken into account, we derive for January an increase in the surface ozone concentration that is generally of the order of 6-8 ppbv (Fig. 11c) in the middle of the country. The change in the photolysis rates reduces the ozone concentration by 2-4 ppbv (Fig. 11a) and compensates to some extent the increase due to aerosol uptake. Such a compensation mechanism was highlighted by Qu et al. (2023) based on their model study performed in the Yangtze River Delta region for different seasons. The combined effect in winter is therefore limited, with ozone values increasing by less than 4 ppbv in most regions of China and by less than 6 ppbv in the urban area.

In July, when combining the photolysis and uptake effects (Fig. S20), we derive a decrease in the concentration of NO_2 (up to 10 pptv) and NO (up to 5 pptv) and an increase in the concentration of OH (0.05 pptv) and HO_2 (up to 10 pptv) in eastern China. The response of ozone (Fig. 11b and d) is characterized by a reduction in the surface concentration of about 10 ppbv (or 15%) in most NO_x-limited regions of China. This value may be slightly overestimated in these regions since our calculated concentrations of aerosol are somewhat higher than the observed values. In the metropolitan areas of Shanghai and Beijing, an increase of about 8 ppbv (or about 12%) is calculated.

These results highlight that, during summertime, the presence of aerosol particles leads to a decrease of the surface O_3 concentrations in NO_x-limited areas whereas it produces an increase in the ozone level in the VOC-limited (metropolitan) areas. Figure 12 presents a schematic view of different pathways that characterize the effects of aerosols on ozone concentrations. Specifically, this figure suggests that the reduction in the aerosol burden that has occurred in China in recent years should have produced an increase in surface ozone concentrations in NO_x-limited areas and a decrease in VOC-limited areas. The cause of the ozone increase in NO_x-sensitive areas should not

be attributed exclusively to a reduction of the HO_2 uptake but to a combination of the different uptake processes and a reduction in the light extinction by the aerosols. The ozone decrease in VOC-limited areas should be mainly attributed to the NO_2 uptake with a counteracting effect by the HO_2 aerosol uptake and by the light extinction by the particles. Our results imply that, if the aerosol loading continues to decrease in the future, the ozone formation will increase so that the air quality measures currently implemented will become less efficient in NO_x-limited areas. This does not imply that ozone will necessarily increase in VOC-limited areas. With a further reduction in the NO_x emissions, which tends to shift the O_3 formation regimes from VOC-limited to NO_x-limited (Tan et al., 2022), the O_3 response to aerosol effects may gradually reverse in these geographical areas.

5.4. Effects of other HONO sources on ozone.

Figure 11e-f shows the changes in the surface ozone concentration due to all sources of HONO considered in the model, including direct emissions from transportation, gas phase production, and heterogeneous reactions of NO_2 uptake on aerosol surfaces and on ground surfaces. In January, the increase of the ozone concentration due to all these different processes reaches 9 ppbv and is more pronounced than in the "aerosol-only" case shown in Fig. 10e. In July, the decrease in the ozone concentration in eastern China (8-10 ppbv) and the increase in the metropolitan regions of Beijing and Shanghai (6-8 ppbv) are about 50% larger than when only the aerosol uptake of NO_2 is taken into account (see Fig. 10f).

Figure 11g-h also shows the changes in the surface ozone concentrations when all heterogeneous reactions involving HO_2, NO_2, NO_3, and N_2O_5 as well as all sources of HONO are included in the model calculation. These two panels (g and h) must be compared with panels (c and d) of Fig. 11. With the additional formation processes of HONO, surface ozone is increased by about 6-8 ppbv in southeastern China during winter. For summer conditions, surface ozone concentration is reduced by up to 10 ppbv in the eastern and southern parts of China, but is increased by about 6-8 ppbv in the two major metropolitan centers.

6. Quantification of the oxidizing capacity of the atmosphere in China

6.1. OH reactivity

The model results presented above allow us to quantify the different factors that characterize the oxidizing capacity of the atmosphere in China. We first analyze the geographical distribution of the OH reactivity (Eq. 8a and 8b) resulting from the reaction of this radical with VOCs and CO (noted VOC^R (Fig. 13a-b)) as well as NO_x (noted NO_x^R (Fig. 13c-d)). These quantities, and particularly the VOC^R/NO_x^R ratio (Fig. 13e-f), can be viewed as a proxy representing the competition between radical production and destruction (see Kirchner et al., 2001).

During winter, the calculated value of the daytime averaged VOC^R ranges from typically 2 s^{-1}, mostly in rural areas, to 10 s^{-1} in the North China Plain between the urban areas of Shanghai and Beijing, as well as in the area of Chengdu. The high value of calculated VOC^R in urbanized areas is consistent with high values in the spatial distribution of wintertime VOCs, such as ethene (Fig. S5), ethane (Fig. S5), and HCHO (Fig. S4). The values derived for the daytime averaged NO_x^R are of the order of 10 s^{-1} in the North China Plain and most metropolitan areas of the country. Values are close to 1 s^{-1} in rural areas. The VOC^R/NO_x^R ratio is of the order of 2 in most regions of China except in the polluted areas where values close to 0.6 to 1 are derived.

During summer, the daytime averaged VOC^R parameter reaches values close to or higher than 10 s^{-1} in southern China. This distribution of these high values is consistent with the spatial distribution of isoprene (Fig. S5) and HCHO (Fig. S4). The value of NO_x^R is smaller than in wintertime with values generally close to 5 s^{-1} in the North China Plain, and approaching 10 s^{-1} inside the cities of Beijing, Shanghai, Guangzhou, and Chengdu. The VOC^R/NO_x^R ratio is larger than 2 in the entire spatial domain, except in a small polluted area of the North China Plain and in the urban areas of Guangzhou and Shanghai where it is close to 1. Figure S21 shows the diurnal variation of the simulated value of the VOC^R to NO_x^R ratio at different sites in January and July of 2018. The daytime values range from 0.5 to 1.8 in urban sites in both two months, with the highest daytime value shown in the Wangdu site in July (by the value of 5).

The diurnal variations of the OH reactivities due to different organic compounds, CO and nitrogen dioxide in January and July are shown in Fig. 14. These calculated values need to be compared with the data provided by the observations. In city sites, for example, Whalley et al. (2021) reported diurnal variations of the OH reactivity in Beijing during the summer of 2018 with values of 25-35 s^{-1} to be compared to our model values of 23-42 s^{-1} in July. Based on measurements, the contribution to the OH reactivity of NO$_x$ reactions is 40-50%, and of VOCs reactions 40-50%. The corresponding values derived in our model study in July are 50% and 45%, respectively. In Shanghai during summertime, Zhu et al. (2021) derived values of 10-25 s^{-1}, where the contribution of the reaction of OH with NO$_x$ is 33%, with CO is 26%, with OVOCs is 18%, and with alkenes is 15%. The reactivity value derived by our model is 10-17 s^{-1}, with the highest contribution from the reaction of OH with NO$_x$ (50-60%). The values measured by Tan et al. (2018) in Chengdu (September 2016) are in the range of 15-30 s^{-1} to be compared to our July model values of 12-32 s^{-1}. During the campaign that took place in Shenzhen in the autumn of 2018, Yang et al. (2022) derived a total OH reactivity value that varied between 10 and 25 s^{-1}, which is relatively lower than our calculated value by 20-45 s^{-1} in Guangzhou in summer.

Several other attempts have been made to derive the OH reactivity from in situ observations in rural sites. At Wangdu during summertime, Tan et al. (2017) derived a reactivity value of 12-23 s^{-}

[1], and our model study provides a value of 8-22 s^{-1}. Tan et al. (2019), refer to the campaign conducted at the Heshan site in the autumn of 2014, derived experimentally mean daytime OH reactivities that range from 20 to 40 s^{-1}, with the contributions with CO, NMHCs, and NO_x, are 10% (2-4 s^{-1}), 20% (4-8 s^{-1}), and 14% (3-6 s^{-1}), respectively. The value of VOC^R and NO_x^R in our model account for approximately 1 to 5 s^{-1} and 2 to 5 s^{-1}, respectively. The underestimation of the HONO concentration in our model (Table S5), contributes to the underestimation of the calculated value of the OH radical and the OH reactivity.

Generally, in winter (Fig. 14a), the dominant contribution to OH reactivity in urban/rural sites is through the reaction of OH and NO_x (40~60%), while, at a remote site (Waliguan) is from the reaction between OH and CO (80%). In summer (Fig. 14b), the contribution of NO_x to OH reactivity is still high in urban/rural sites (40~70%), with one exception at the Heshan site. At this site, the largest reactivity of OH results from the reaction with alkene (40~50%), which is associated with the relatively low value of NO_x (Fig. S1d) and high value of isoprene (Fig. S5) at this site.

We also show in Fig. 15 three other indicators; these describe the catalytic cycling of NO_x leading to ozone formation until the chain reaction is interrupted: the radical chain length *ChL* (defined by Eq. 9), the ozone production efficiency *OPE* (defined by Eq. 11), and the atmospheric oxidation capacity *AOC* (defined by Eq. 15).

6.2. Chain Length *(ChL)*

The value of the daytime averaged *ChL*, which, according to our definition, increases with the atmospheric concentration of RO_x radicals and NO, is of the order of 3 to 5 cycles in remote areas. In January (Fig. 15a), *ChL* reaches values as high as 8 to 10 cycles in the southern area of China. The *ChL* values are low in northern and western China, where the NO concentrations are low during winter. In July (Fig. 15b), the highest values of *ChL* (about 10 cycles) are found only in the metropolitan areas, where the HO_x concentrations are high. Since this parameter can be viewed as the ratio between the ozone and RO_x production rate (see Eq. 11), the polluted areas tend to favor ozone production for a given value of the RO_x formation rate. Examples of the diurnal variation of the chain length are provided in Fig. S22 in the Supplementary Information.

A few experimental estimates are available to quantify the value of the chain length: Zhu et al. (2021) derived a value of 2-6 for daytime *ChL* in Shanghai during the warm season of 2018 to be compared to the values of 4-5 provided by our model (Fig. S23). Yang et al. (2021) derive daytime values of 2-4.5 in Chengdu during summer, while our model provides values close to 4-5. In Guangzhou during summer, Wang et al. (2022) derive daytime values of 3-12 in fair agreement with our calculated values of 6-10. This discrepancy of *ChL* in city sites can be partially explained by the overestimation in relevant NO_2 concentrations.

6.3. Ozone production efficiency (*OPE*)

The Ozone Production Efficiency (*OPE*) represents the number of ozone molecules produced by NO$_x$ before NO$_x$ is further oxidized to form more stable nitrogen reservoirs or removed from the atmosphere by deposition. The daytime averaged *OPE* values are highest (larger than 30) in the southwest of China and are of the order of 25-30 above the Tibetan plateau (Fig. 15C-d) in both seasons. *OPE* values typically ranges between 3 to 15 in the eastern plain during both months under consideration. We note the similarities suggested by Eq. (14) between the distributions of *OPE* and of the VOC^R/NO_x^R ratio in the VOC-limited regions of the China Northern Plain and over the Eastern China Sea where the effects of ship emissions are visible. Daytime *OPE* values are usually low at urban sites. More details on the diurnal variation of the *OPE* are provided in Fig. S24 of the Supplementary Information.

A few experimental data characterizing the *OPE* are available: Wang et al. (2017) summarize the summertime *OPE* values derived in China between 2006 and 2015 with values ranging from 2.1 to 20.2, which is comparable with our results that range from 1 to 30.

6.4. Atmospheric Oxidizing Capacity (*AOC*)

Finally, we show in Fig. 15e-f the spatial distribution of the daytime averaged value of the atmospheric oxidizing capacity *AOC* in January and July, respectively. In winter, the highest daytime values of *AOC* are found in the southern part of China, especially in the Pearl River Delta region (3×10^7 cm^{-3} s^{-1}). During nighttime (Fig. S25), the *AOC* values are lower than 0.2×10^7 cm^{-3} s^{-1}, with maximum values found at the southern coast of China. These high *AOC* values are associated with the spatial distribution of wintertime formaldehyde (Fig. S4), isoprene (Fig. S5), and of the HO$_x$ and NO$_3$ radicals (Fig. S6). In summer, the values of daytime *AOC* are highest in the metropolitan urban areas (up to 10×10^7 cm^{-3} s^{-1}), particularly in the vicinity of Beijing. The nocturnal *AOC* values are lower than 2×10^7 cm^{-3} s^{-1} (Fig. S25) with high spots found in urban areas. The distribution of summertime *AOC* has some resemblance with the distribution of nitrogen species, including NO$_2$ (Fig. S1) and HONO (Fig. S4).

Figure 16 shows the diurnal evolution of the *AOC* and the dominant photochemical processes that contribute to this quantity in different urban and rural areas for January and July, respectively. First, we note that, in January, the noontime value of *AOC* does not supersede 6×10^7 cm^{-3} s^{-1} in urban areas and 3×10^7 cm^{-3} s^{-1} at rural sites (where the value is lower than 1.5×10^7 cm^{-3} s^{-1} in most cases). At the remote high-altitude station of Waliguan in western China (remote conditions), the maximum *AOC* value is lower than 0.2×10^7 cm^{-3} s^{-1}. In July, as expected, the oxidizing capacity is larger than in winter, with noontime values reaching $(15-20)\times10^7$ cm^{-3} s^{-1} in metropolitan areas but limited increase in rural and remote areas. The increasing summertime *AOC* in city sites is

1030　attributed to the larger value of *AOC* contributed by OVOCs and alkene, which is associated with the higher value of summertime OVOCs (Fig. S4) and isoprene (Fig. S6) in urban areas.

Additional information on the relative contribution of different photochemical processes as a function of the time of the day and for two seasons is provided in Fig. 17. During winter, in Beijing

1035　during daytime, the major contributions to *AOC* are provided by the reaction of OH with alkenes, aromatics, and carbon monoxide. The situation is similar in the other three metropolitan areas under consideration. In Chengdu, however, the relative contribution of CO is larger as is the case at rural sites where the concentration of hydrocarbons is generally low. At night, the largest contribution in Beijing, Shanghai, and Chengdu is provided by the oxidation of hydrocarbons by

1040　ozone.

During summertime, the daytime value of *AOC* in urban regions is determined by the reaction of OH with alkenes and with OVOCs. In remote areas, the dominant contribution is attributed to the reaction of OH with OVOCs and with CO. OVOCs are produced as a result of the oxidation of

1045　biogenic hydrocarbons such as isoprene, primarily but not exclusively in rural areas, and by the oxidation of anthropogenic hydrocarbons, mostly in urban and industrialized areas. Thus, any analysis of the processes that determine the value of *AOC*, particularly during summertime, must take into account the role played by OVOCs. Li et al. (2023) reported that the OVOCs have a significant impact on the atmospheric oxidative capacity in the Yangtze River Delta region, through reactions

1050　with OH during daytime and with NO_3 at night. Due to the limited amount of measurement data available (Wang W. et al., 2022), and the high uncertainties in the emissions of organic species (Li et al., 2023), the contributions of specific OVOCs to the oxidative process are still not unclear. More work is needed to obtain a better understanding of the impact of OVOCs on the oxidative processes in China.

1055

In all regions under consideration, during summertime, a dominant nighttime contribution to the value of *AOC* is provided by the oxidation of hydrocarbons by NO_3. As the production of NO_3 occurs through the reaction of O_3 and NO_2, the higher summertime O_3 concentrations and temperature lead to the larger formation of NO_3 than during winter. Wang H. (2023) highlights the in-

1060　creasingly critical role of NO_3-related nighttime oxidative chemistry associated with the positive trend in particulate nitrate abundance and in the formation of O_3 and other secondary pollutants. With the reduction in NO_x emissions, the importance of NO_3 radicals may become more notable.

The model study confirms that, during daytime, more than 90% of *AOC* is due to reactions of

1065　chemical species with the OH radical. During nighttime, the oxidation processes are considerably slower and are due principally to the reactions of hydrocarbons with the nitrate radical (NO_3) and alkenes with ozone (O_3). In urban areas, the dominant daytime contributions to *AOC* during summertime are the reactions with carbon monoxide (20%), alkenes (35%), aromatics (10%), and OVOCs (30%). During winter, the corresponding numbers are 25% for carbon monoxide, 40% for

1070   alkenes, 15% for aromatics, and 15% for OVOCs, respectively. These approximate values vary somewhat from city to city. At night, during summer, the major contributions in urban areas are the oxidation by NO_3 (60% in Beijing, 45% in Chengdu, 15% in Shanghai and Guangzhou) and ozone (20% in Beijing, 35% in Shanghai, and 25% in Chengdu). At the very remote station of Waliguan, the relative daytime contributions to *AOC* in summer are 25% due to CO, 20% due to

1075   methane, 40% due to OVOCs, and 10% due to alkenes. The corresponding contributions during winter are 60% for CO, 20% for methane, 10% for OVOCs, and 5% for alkenes.

These model values can be compared, for example, with values calculated by Zhu et al. (2020) from experimental data obtained in Shanghai. The peak value around noontime in summer is about

1080 $(5-10)\times10^7$ cm^{-3} s^{-1} in fair agreement with our estimates. In the wintertime, the values are between $(5-8)\times10^7$ cm^{-3} s^{-1}, i.e., slightly higher than our calculated *AOC*. Feng et al. (2021) report a maximum value of about 1.7×10^8 cm^{-3} s^{-1} for the *AOC* at urban sites in Beijing during the summertime of 2014. This number is close to our calculated value of *AOC* by 1.8×10^8 cm^{-3} s^{-1} in July. The peak *AOC* value of 2.1×10^7 cm^{-3} s^{-1} reported by Liu et al. (2021) for the winter of 2018 in Beijing is

1085   close to the model value of 3×10^7 cm^{-3} s^{-1}.

7. Summary and Conclusions

The oxidizing capacity of the atmosphere can be characterized by different parameters including

1090   the production and destruction rates of ozone and other oxidants, the ozone production efficiency, the OH reactivity, and the length of the reaction chain responsible for the formation of ozone and RO_x. The value of these parameters depends on whether ozone formation is limited by the availability of NO_x or VOCs. It is also affected by the aerosol burden in the atmosphere, specifically by the rate at which heterogeneous chemical reactions take place in the atmosphere. In the present

1095   study, we have used a regional chemical transport model with a detailed chemical scheme to quantify these parameters in several chemical environments in China. Such studies should be helpful in determining the factors that are responsible for the documented changes in the oxidation capacity of the atmosphere and hence the mean concentration of surface ozone in different regions of the country.

1100

Our study shows that during winter, the formation of ozone in most of the eastern China Plain is VOC-limited. The ozone formation in remote western regions of the country, however, is NO_x-limited. In the south, an intermediate situation prevails, except in the Pearl River Delta area, where the formation of ozone is VOC-limited. In summer, ozone formation is NO_x-limited in most re-

1105   gions of China except in the urban areas of Beijing, Shanghai, Guangzhou, and Chengdu.

Our model calculations conducted for the summer season show that the largest contribution to the formation of RO_x radicals in rural areas is due to the photolysis of ozone followed by the reaction between the electronically excited oxygen atom with water vapor. The second largest contribution

1110 is provided by the photolysis of formaldehyde. In urban and suburban areas, the formation of RO_x starts in the early morning with the photolysis of HONO, followed by the photolysis of HCHO and other OVOCs and finally of ozone. In polluted areas, the contribution of oxygenated VOCs is important and needs to be included in any oxidant budget analysis.

1115 The summertime destruction of RO_x radicals in the rural regions is principally due to radical-radical reactions, including $HO_2 + HO_2$, $HO_2 + RO_2$, and $HO_2 + OH$. In urban and suburban areas, the main destruction processes are associated with reactions between NO_2 and OH, and between RO_2 and NO. The destruction of radicals associated with the uptake of HO_2 on aerosol surfaces plays a limited role.

1120

At all the considered sites, the production rate of ozone is due about equally to the reactions of NO with HO_2 and RO_2, respectively. The source of RO_2 varies according to the region; it is mostly anthropogenic in urban areas and biogenic in remote areas. Values of ozone production rate are substantially higher in metropolitan areas than in remote areas: the maximum value in the early

1125 afternoon reaches 100 ppbv h^{-1} in Beijing and Shanghai but is less than 2 ppbv h^{-1} at the rural sites.

Our model simulations suggest that heterogeneous chemistry together with the effect of aerosol on light extinction (photolysis) contribute to an increase in the surface ozone concentrations by 4-6 ppbv during wintertime. In summer, the presence of the aerosol burden derived by our model leads

1130 to a reduction in surface ozone of up to 8 ppbv in the NO_x-limited areas of the central and eastern parts of China. The ozone concentrations, however, are enhanced by about 5-7 ppbv in the VOC-limited regions near Shanghai and Beijing. The reduction in the aerosol burden, resulting from the measures taken by Chinese authorities, will therefore lead to an increase of the O_3 density in the NO_x-limited rural areas and affect the efficiency of O_3 pollution control. A decrease of the O_3

1135 concentration is expected in the VOC-limited areas. However, with the continuous reduction in NO_x emissions, the NO_x-limited areas tend to geographically expand, and an O_3 increase should therefore occur in a broader area.

The daytime averaged OH reactivity due to NO_x varies from less than 1 s^{-1} in the western part of

1140 the country to 10 s^{-1} in the North China Plain during winter. It is closer to 3 s^{-1} during summer except in large urban areas where it is close to 10 s^{-1}. The reactivity due to VOCs is very small in the western regions of the country, but varies from 2 to 10 s^{-1} in eastern China, with somewhat higher values in winter. The VOC^R-to-NO_x^R ratio is higher than 5 over the Tibetan Plateau, but less than 1.5 in the eastern regions of the country and even smaller in NO_x-rich regions of the most

1145 polluted areas.

The number of cycles affecting RO_x radicals during the daytime before they undergo a termination process is around 3 to 5 in remote areas. In January, it reaches 8 to 10 cycles in the eastern plain and in the southern area of China. The values are low in northern and western China, where the

1150 NO concentration is low during winter. In the metropolitan areas during July, about 10 cycles are performed before the radicals are lost.

Finally, our model simulations suggest that the daytime oxidizing capacity is mostly influenced by the reaction of the OH radical with alkenes, carbon monoxide, and oxygenated VOCs, and to a
1155 lesser extent with aromatics. The relative contribution of different chemical processes varies with locations (urban versus rural) and with seasons (winter versus summer). During nighttime, the largest contributions are due to the oxidation of hydrocarbons by NO_3 and ozone.

The results reported in the present study are not exempt from uncertainties associated, for example,
1160 with the adopted surface emissions of primary species and the coarse spatial resolution of the model grid. One particularly important uncertainty is associated with the calculation of the VOC concentrations. The emissions of these organic species remain uncertain and the adopted VOC oxidation mechanism, partly based on the model on the definition of lumped species, are the sources of errors in the calculated values of the OH reactivity and of the atmospheric oxidation
1165 capacity.

With the reduction of NO_x emissions observed in China, explicit consideration of nocturnal oxidative chemistry taking into account, the effect of nitrate radicals will become increasingly crucial for the assessment of air quality. With the reduction in the anthropogenic emissions of VOCs in China, the role of natural VOCs with high reactivity, such as isoprene, will become increasingly
1170 important regarding oxidative processes, especially in scenarios with increasing temperatures and extreme weather associated with climate change. Future work will focus on the role of emission changes on the photo-oxidative species and parameters. To understand the contribution of photo-degradable OVOCs to the oxidative capacity of the atmosphere and to the formation of secondary pollutants, additional studies that include systematic measurements of OVOCs and more accurate
1175 time-dependent estimates of emissions will be needed.

Code and data availability. The WRF-Chem model is publicly available at https://www2.mmm.ucar.edu/wrf/users/. The air quality data at surface stations are publicly avail-
1180 able at the website of the Ministry of Ecology and Environment of the People's Republic of China at http://english.mee.gov.cn/.

Author contributions. JD and GB designed the structure of the manuscript, performed the numer-
1185 ical experiments, analyzed the results, and wrote the manuscript. JD analyzed the data and established the figures. All co-authors provided comments and reviewed the manuscript.

1190

1195

References

1200

Abdi-Oskouei, M., Roozitalab, B., Stanier, C. O., Christiansen, M., Pfister, G., Pierce, R. B., et al. The impact of volatile chemical products, other VOCs, and NO_x on peak ozone in the Lake Michigan region. Journal of Geophysical Research: Atmospheres, 127, e2022JD037042. https://doi.org/10.1029/2022JD037042, 2022.

1205

Bertram, T. H. and Thornton, J. A.: Toward a general parameterization of N_2O_5 reactivity on aqueous particles: the competing effects of particle liquid water, nitrate, and chloride, Atmos. Chem.Phys., 9, 8351–8363, https://doi.org/10.5194/acp-9-8351-2009, 2009.

1210   Brown, S. S., and Stutz, J. Nighttime radical observations and chemistry. Chemical Society Reviews, 41(19), 6405– 6447. https://doi.org/10.1039/C2CS35181A, 2012.

Czader, B. H., Rappenglück, B., Percell, P., Byun, D. W., Ngan, F., and Kim, S., Modeling nitrous acid and its impact on ozone and hydroxyl radical during the Texas Air Quality Study 2006, Atmos. Chem. Phys., 12, 6939-6951, https://doi.prg/10.5194'acp12-6939-2012, 2012.

1215

Chin, M., Ginoux, P., Kinne, S., Torres, O., Holben, B. N., Duncan, B. N., Martin, R. V., Logan, J. A., Higurashi, A., Nakajima, T. Tropospheric Aerosol Optical Thickness from the GOCART Model and Comparisons with Satellite and Sun Photometer Measurements, Journal of the Atmospheric Sciences, 59(3), 461-483., https://doi.org/10.1175/1520-0469(2002)059, 2002.

1220

Dai, J., Liu, Y., Wang, P., Fu, X., Xia, M., Wang, T. The impact of sea-salt chloride on ozone through heterogeneous reaction with N2O5 in a coastal region of south China. Atmospheric environment, 236, 117604. https://doi.org/10.1016/j.atmosenv.2020.117604, 2020.

1225

Dai, J. and Wang, T.: Impact of international shipping emissions on ozone and PM$_{2.5}$ in East Asia during summer: the important role of HONO and ClNO$_2$, Atmos. Chem. Phys., 21, 8747–8759, https://doi.org/10.5194/acp-21-8747-2021, 2021.

1230 Dyson J. E., et al., Impact of HO$_2$ aerosol uptake on radical levels and O$_3$ production during summertime in Beijing, Atmos. Chem. Phys. Discussions, https://doi.org/10.5194/acp-2022.800, 2022.

Elshorbany, Y. F., R. Kurtenbach, P. Wiesen, E. Lissi, M. Rubio, G. Villena, E. Gramsch, A. R. Rickard, M. J. Pilling, and J. Kleffmann, Oxidation capacity of the city air of Santiago, Chile,

1235 Atmos. Chem. Phys., 9, 2257–2273, https://doi.org/10.5194/acp-9-2257-2009, 2009.

Elguindi, N., Granier, C., Stavrakou, T., Darras, S., Bauwens, M., Cao, H., et al. Intercomparison of magnitudes and trends in anthropogenic surface emissions from bottom-up inventories, top-down estimates, and emission scenarios. Earth's Future, 8, e2020EF001520.

1240 https://doi.org/10.1029/2020EF001520, 2020.

Emmons, L. K., Walters, S., Hess, P. G., Lamarque, J.-F., Pfister, G. G., Fillmore, D., Granier, C., Guenther, A., Kinnison, D., Laepple, T., Orlando, J., Tie, X., Tyndall, G., Wiedinmyer, C., Baughcum, S. L., and Kloster, S.: Description and evaluation of the Model for Ozone and Related chem-

1245 ical Tracers, version 4 (MOZART-4), Geosci. Model Dev., 3, 43–67, https://doi.org/10.5194/gmd-3-43-2010, 2010.

Fast, J. D., Gustafson, W. I., Easter, R. C., Zaveri, R. A., Barnard, J. C., Chapman, E. G., Grell, G. A., and Peckham, S. E., Evolution of ozone, particulates, and aerosol direct radiative forcing in

1250 the vicinity of Houston using a fully coupled meteorology-chemistry-aerosol model, J. Geophys. Res., 111, D21305, https://doi.org/10.1029/2005JD006721, 2006.

Feng, T., Zhao, S., Hu, B., Bei, N., Zhang, X., Wu, J., Li, G. Assessment of Atmospheric Oxidizing Capacity Over the Beijing-Tianjin-Hebei (BTH) Area, China. Journal of Geophysical Research:

1255 Atmospheres, 126(7),https://doi.org/10.1029/2020JD033834, 2021.

Fu, X., Wang, T., Zhang, L., Li, Q., Wang, Z., Xia, M., Yun, H., Wang, W., Yu, C., Yue, D., Zhou, Y., Zheng, J., and Han, R.: The significant contribution of HONO to secondary pollutants during a severe winter pollution event in southern China, Atmos. Chem. Phys., 19, 1–14,

1260 https://doi.org/10.5194/acp-19-1-2019, 2019.

Fu, X., Wang, T., Gao, J., Wang, P., Liu, Y., Wang, S., Persistent heavy winter nitrate pollution driven by increased photochemical oxidants in northern China. Environmental Science & Technology, 54(7), 3881–3889. https://doi.org/10.1021/acs.est.9b07248, 2020.

1265

Gaubert, B., L. K. Emmons, K. Raeder., Correcting model biases of CO in East Asia: impact on oxidant distributions during KORUS-AQ, Atmos. Chem. Phys., 20, 14617-14647, https://doi.org/105194/acp-20-14617-2020, 2020.

1270 Granier, C., Darras, S., Denier van der Gon, H., Doubalova, J., Elguindi, N., Galle, B., et al.,. The Copernicus atmosphere monitoring service global and regional emissions. Copernicus Atmosphere Monitoring Service (CAMS). https://doi.org/10.24380/d0bn-kx16, 2019.

Guenther, A. B., Jiang, X., Heald, C. L., Sakulyanontvittaya, T., Duhl, T., Emmons, L. K., & 1275 Wang, X. The Model of Emissions of Gases and Aerosols from Nature version 2.1 (MEGAN2.1): An extended and updated framework for modeling biogenic emissions. Geo-scientific Model Development, 5, 1471–1492. https://doi.org/10.5194/gmd-5-1471-2012, 2012.

Grell, G. A., Peckham, S. E., Schmitz, R., McKeen, S. A., Frost, G., Skamarock, W. C., & Eder, 1280 B. Fully coupled "online" chemistry within the WRF model. Atmos. environ. , 39(37), 6957-6975. https://doi.org/10.1016/j.atmosenv.2005.04.027, 2005.

Geyer, A., Alicke, B., Konrad, S., Schmitz, T., Stutz, J. and Platt, U.: Chemistry and oxidation capacity of the nitrate radical in the continental boundary layer near Berlin, J. Geophys. Res., 106, 1285 8013–8025, https://doi.org/10.1029/2000JD900681, 2001.

Ivatt, P. D., M. J. Evans, and A. C. Lewis, Suppression of surface ozone by an aerosol-inhibited photochemical ozone regime, Nature Geoscience, https://doi.org/10.1038/s41561-022-00972-9, 2022

1290 Jacob, D. J.: Heterogeneous chemistry and tropospheric ozone, Atmos. Environ., 34, 2131-2159, https://doi.org/10.1016/S1352-2310(99)00462-8, 2000.

Kirchner, F., Jeanneret, F., Clappier, A., Krüger, B., van den Bergh, H., Calpini, B. Total VOC 1295 reactivity in the planetary boundary layer: 2. A new indicator for determining the sensitivity of the ozone production to VOC and NO x. J. Geophys.l Res., 106 (D3), 3095-3110. https://doi.org/10.1029/2000JD900603, 2001.

Lakey, P. S. J., I. J. George, L. K. Whalley, M. T. Baeza-Romero, and D. E. Heard, Measurements 1300 of the HO_2 uptake coefficients onto single component organic aerosols, Environ. Sci., Technol., 49, 4878-4885, https://doi.org/10.1021/acs.est.5b00948, 2015.

Levy, H., Normal atmosphere: large radical and formaldehyde concentrations predicted, Science, 173, 141-143, https://doi.org/10.1126/science.173.3992.14, 1971.

1305

Li, G., W. Lei, M. Zavala, R. Volkamer, S. Dusanter, P. Stevens, and L. T. Molina, Impacts of HONO sources on the photochemistry in Mexico City during the MCMA-2006/MILOGO Campaign, Atmos. Chem. Phys. 10, 6551-6567, https://doi.org/10.5194/acp-10-655102010, 2010.

1310 Li, D. D., Xue, L. K., Wen, L., Wang, X. F., Chen T. S., Mellouki, A. Chen J. M., and Wang W. X., Characteristics and source of nitrous acid in an urban atmosphere in northern China: Results from 1-yr continuous observations, Atmos. Environ., 182, 296-306, https://doi.org/10.1016/j.atmosenv.2018.03.033.2018, 2018.

1315 Li, K.; Jacob, D. J.; Liao, H.; Shen, L.; Zhang, Q.; Bates, K. H., Anthropogenic drivers of 2013−2017 trends in summer surface ozone in China. Proc. Natl. Acad. Sci., 116 (2), 422−427, https://doi.org/10.1073/pnas.1812168116, 2019a.

Li, K.; Jacob, D. J.; Liao, H.; Zhu, J.; Shah, V.; Shen, L.; Bates, K.H.; Zhang, Q.; Zhai, S. A two-
1320 pollutant strategy for improving ozone and particulate air quality in China. Nat. Geosci. 12, 906−910. https://doi.org/10.1038/s41561-019-0464-x, 2019b.

Li, J., Li, X.L., Wang, X., Wang, H., Jing, S., Ying, Q., Qin, M., Hu, J. Fate of oxygenated volatile organic compounds in the Yangtze River Delta Region: source contributions and impacts on the
1325 atmospheric oxidation capacity. Environ. Sci. Technol. 56, 11212–11224. https://doi.org/10.1021/acs.est.2c00038, 2022.

Li, Z., Xue, L., Yang, X., Zha, Q., Tham, Y. J., Yan, C., ... & Wang, W.. Oxidizing capacity of the rural atmosphere in Hong Kong, Southern China. Science of the total environment, 612, 1114-
1330 1122.https://doi.org/10.1016/j.scitotenv.2017.08.310, 2018.

Liu, J., Li, X., Tan, Z., Wang, W., Yang, Y., Zhu, Y., Yang, S., Song, M., Chen, S., Wang, H., Lu, K., Zeng, L., and Zhang, Y.: Assessing the ratios of formaldehyde and glyoxal to NO2 as Indicators of O3–NOx–VOC sensitivity, Environ. Sci. Technol., 55, 10935–10945,
1335 https://doi.org/10.1021/acs.est.0c07506, 2021.

Liu, P., Xue, C., Ye, C., Liu, C., Zhang, C., Wang, J., Mu, Y. The Lack of HONO Measurement May Affect the Accurate Diagnosis of Ozone Production Sensitivity. ACS Environ. Au, https://doi.org/10.1021/acsenvironau.2c00048, 2022.
1340
Liu, T., Hong, Y., Li, M., Xu, L., Chen, J., Bian, Y., Yang, C., Dan, Y., Zhang, Y., Xue, L., Zhao, M., Huang, Z., and Wang, H.: Atmospheric oxidation capacity and ozone pollution mechanism in a coastal city of southeastern China: analysis of a typical photochemical episode by an observation-based model, Atmos. Chem. Phys., 22, 2173–2190, https://doi.org/10.5194/acp-22-2173-2022,
1345 2022.

Liu, Y. and Wang Tao, Worsening urban ozone pollution in China from 2013 to 2017 – Part 2: The effects of emission changes and implications for multi-pollutant control, Atmos. Chem. Phys., 20, 6323-6337, https://doi.org/10.5194/acp-206323, 2020.

1350

Liu Y., Lu K., Li, X., Dong H., Tan Z. Wang, H., Zou, Q., Wu, Y., Hu, M., Min, K.-E., Kecorius, S., Wiendensohler, A., and Zhang Y., A comprehensive model test of the HONO sources constrained to field measurements at rural North China Plain, Environ. Sci., Technol. 53, 3517-3525, https://doi.org/10.1021/acs.est.8b06367, 2019.

1355

Liu, Z., Wang, Y., Hu, B., Lu, K., Tang, G., Ji, D., Zhang, Y., Elucidating the quantitative characterization of atmospheric oxidation capacity in Beijing, China. Science of the Total Environment, 771, 145306., https://doi.org/10.1016/j.scitotenv.2021.145306, 2021.

1360 Lu, X., Hong, J. Y., Zhang, L., Cooper, O. R., Schultz, M. G., Xu, X. B., Wang, T., Gao M., Zhao, Y. H., and Zhang, Y. H., Severe surface ozone pollution in China: A global perspective, Environ. Sci. Tech Lett., 5, 487-494, https://doi.org/10.1021/acs.estlett.8b00366, 2018.

Ma, X., Tan, Z., Lu, K., Yang, X., Liu, Y., Li, S., Zhang, Y, Winter photochemistry in Beijing: 1365 Observation and model simulation of OH and HO2 radicals at an urban site. Sci. of the Total Environ., 685: 85-95, https://doi.org/10.1016/j.scitotenv.2019.05.329, 2019.

Mao, J., Ren, X., Chen, S., Brune, W. H., Chen, Z., Martinez, M., Leuchner, M. Atmospheric oxidation capacity in the summer of Houston 2006: Comparison with summer measurements in 1370 other metropolitan studies. Atmospheric Environment, 44(33), 4107-4115. https://doi.org/10.1016/j.atmosenv.2009.01.013, 2010.

Mao, J., Fan, S., Jacob, D. J., Travis, K. R. Radical loss in the atmosphere from Cu-Fe redox coupling in aerosols. Atmospheric Chemistry and Physics, 13(2), 509-519. 1375 https://doi.org/10.5194/acp-13-509-2013, 2013.

Mao, J., Fan, S., Travis, K. R., Horowitz, L. W. Soluble Fe in aerosols sustained by gaseous HO2 uptake. Environmental Science & Technology Letters, 4(3), 98-104. https://doi.org/10.1021/acs.estlett.7b00017, 2017.

1380

Martinez, M., Harder, H., Kovacs, T. A., Simpas, J. B., Bassis, J., Lesher, R., Zamora, R. J.. OH and HO2 concentrations, sources, and loss rates during the Southern Oxidants Study in Nashville, Tennessee, summer 1999. Journal of Geophysical Research: Atmospheres, 108(D19).https://doi.org/10.1029/2003JD003551, 2003.

1385

Martin, R. V., D., J., Jacob, R. M. Yantosca, M. Chin and P. Ginoux, Global and regional decreases in tropospheric oxidants from photochemical effects of aerosols, J. Geophys. Res., 108, https://doi.org/10.1029/2002JD002622, 2003.

1390   Mozurkewich, M., McMurry, P. H., Gupta, A., and Calvert, J. G.: Mass accommodation coefficient of HO2 on aqueous particles, J. Geophys. Res., 92, 4163–4170, https://doi.org/10.1029/JD092iD04p04163, 1987.

Ng, N. L., Brown, S. S., Archibald, A. T., Atlas, E., Cohen, R. C., Crowley, J. N. Nitrate radicals
1395   and biogenic volatile organic compounds: Oxidation, mechanisms, and organic aerosol. Atmospheric Chemistry and Physics, 17(3), 2103– 2162. https://doi.org/10.5194/acp-17-2103-2017, 2017.

Qu, Y., Wang, T., Yuan, C., Wu, H., Gao, L., Huang, C., Xie, M. The underlying mechanisms of
1400   PM2. 5 and O3 synergistic pollution in East China: Photochemical and heterogeneous interactions. Science of The Total Environment, 873, 162434. https://doi.org/10.1016/j.scitotenv.2023.162434, 2023.

Prinn, R. G., The cleansing capacity of the atmosphere, Annu. Rev. Environ. Resour., 28, 29-57,
1405   https://doi:10.1146/annurev.energy.28.011503.163425, 2003.

Schwarz, H. A., Bielski, B. H., Reactions of hydroperoxy and superoxide with iodine and bromine and the iodide (I2-) and iodine atom reduction potentials. The Journal of Physical Chemistry, 90(7), 1445-1448.https://doi/pdf/10.1021/j100398a045, 1986.
1410
Schwartz, S. E., Mass-transport considerations pertinent to aqueous phase reactions of gases in liquid water clouds, in Chemistry of Multiphase Atmospheric System, NATO ASI Ser. Ser. G., vol6, edited by W. Jaeschke, pp. 415-471, Springer, New York. https://doi/10.1007/978-3-642-70627-1_16, 1986.
1415
Song, H., X. Chen, K. Lu et al., Influence of aerosol copper on HO2 uptake: a novel parameterized equation, Atmos. Chem. Phys., 20 15835-15850, https://doi.org/10.5194/acp-20-15835-2020, 2020.

1420   Song, H., Lu, K., Dong, H., Tan, Z., Chen, S., Zeng, L., & Zhang, Y. Reduced aerosol uptake of hydroperoxyl radical may increase the sensitivity of ozone production to volatile organic compounds. Environmental Science & Technology Letters, 9(1), 22-29. https://doi.org/10.1021/acs.estlett.1c00893, 2021.

1425   Ridley, B., Nitrogen compounds, in Brasseur G. P., J. J. Orlando and G. S. Tyndall, Atmospheric Chemistry and Global Change, Oxford University Press, pp.235-289, 1999.

Skamarock, W.C.; Klemp, J.B.; Dudhia, J.; Gill, D.O.; Liu, Z.; Berner, J.; Wang, W.; Powers, J.G.; Duda, M.G.; Barker, D.M.; et al. A Description of the Advanced Research WRF Model Version
1430   4; Mesoscale and Microscale Meteorology Laboratory NCAR: Boulder, CO, USA, 2019.

Tan, Z., Fuchs, H., Lu, K., Hofzumahaus, A., Bohn, B., Broch, S., Zhang, Y. Radical chemistry at a rural site (Wangdu) in the North China Plain: observation and model calculations of OH, HO_2 and RO_2 radicals. Atmos. Chem. Phys., 17(1), 663-690., https://doi.org/10.5194/acp-17-663-201,
1435   2017.

Tan, Z., Lu, K., Jiang, M., Su, R., Dong, H., Zeng, L., Zhang, Y. Exploring ozone pollution in Chengdu, southwestern China: A case study from radical chemistry to O3-VOC-NOx sensitivity. Science of the Total Environment, 636, 775-786. https://doi.org/10.1016/j.scitotenv.2018.04.286,
1440   2018.

Tan, Z., Lu, K., Hofzumahaus, A., Fuchs, H., Bohn, B., Holland, F., Liu, Y., Rohrer, F., Shao, M., Sun, K., Wu, Y., Zeng, L., Zhang, Y., Zou, Q., Kiendler-Scharr, A., Wahner, A., and Zhang, Y.: Experimental budgets of OH, HO_2, and RO_2 radicals and implications for ozone formation in the
1445   Pearl   River   Delta   in   China   2014,   Atmos.   Chem.   Phys.,   19,   7129–7150, https://doi.org/10.5194/acp-19-7129-2019, 2019.

Tan, Z., A. Hofzumahaus, K. Lu, S. S. Brown, F. Holland, L. G. Huey, A. Kiendler-Scharr, X. Li, X. Liu, and N. Ma, No evidence for a significant impact of heterogeneous chemistry on radical
1450   concentrations in the northern China Plain in summer 2014, Environ. Sci., Technol., 54, 5973-5979, https://doi.org/10.1021/acs.est.0c00525, 2020.

Tan, Z., Lu, K., Ma, X., Chen, S., He, L., Huang, X., Zhang, Y. Multiple Impacts of Aerosols on O3 Production Are Largely Compensated: A Case Study Shenzhen, China. Environmental Science
1455   & Technology, 56(24), 17569-17580, https://doi.org/10.1021/acs.est.2c06217, 2022.

Tie, X., G. Brasseur, L. Emmons, L. Horowitz, and D. Kinnison, Effects of aerosols on tropospheric oxidants: A global model study, J. Geophys. Res., 106, 2931-2964, https://doi.org/10.1029/2001JD900206, 2001.
1460
Tie, X., S. Madronich, S. Walters, D. P. Edwards, P. Ginoux, N. Mahowald, R. Y. Zhang, C. Lou and G. Brasseur, Assessment of the global impact of aerosols on tropospheric oxidants, J. Geophys. Res., 110, D03204, https://doi.org/10.1029/2004JD005359, 2005.

Tie, X., Brasseur, G., and Ying, Z.: Impact of model resolution on chemical ozone formation in Mexico City: application of the WRF-Chem model, Atmos. Chem. Phys., 10, 8983–8995, https://doi.org/10.5194/acp-10-8983-2010, 2010.

Thornton, J. A., Kercher, J. P., Riedel, T. P., Wagner, N. L., Cozic, J., Holloway, J. S., ... & Brown, S. S. A large atomic chlorine source inferred from mid-continental reactive nitrogen chemistry. Nature, 464(7286), 271-274.https://doi.org/10.1038/nature08905, 2010.

Thompson, A. M., The oxidizing capacity of the earth's atmosphere: Probable past and future changes, Science, 256, 1157-1165, https://doi.org/10.1126/science.256.5060.1157, 1992.

Tonnesen, G. S. & Dennis, R. L. Analysis of radical propagation efficiency to assess ozone sensitivity to hydrocarbons and NOx: 1. Local indicators of instantaneous odd oxygen production sensitivity. Journal of Geophysical Research, 105, 9213−9225. https://doi.org/10.1029/1999jd900371, 2000.

Whalley, L. K., Slater, E. J., Woodward-Massey, R., Ye, C., Lee, J. D., Squires, F., Heard, D. E.,. Evaluating the sensitivity of radical chemistry and ozone formation to ambient VOCs and NOx in Beijing. Atmospheric Chemistry and Physics, 21(3), 2125-2147. https://doi.org/10.5194/acp-21-2125-2021, 2021.

Wang, H., Wang, H., Lu, X., Lu, K., Zhang, L., Tham, Y. J., Zhang, Y. Increased night-time oxidation over China despite widespread decrease across the globe. Nature Geoscience, 1-7. https://doi.org/10.1038/s41561-022-01122-x, 2023.

Wang, P., Zhu, S., Vrekoussis, M., Brasseur, G. P., Wang, S., & Zhang, H. Is atmospheric oxidation capacity better in indicating tropospheric O_3 formation, Front. Environ. Sci., Eng., 16(5): 65, https://doi.org/10.1007/s11783-022-1544-5, 2022.

Wang, W., Yuan, B., Peng, Y., Su, H., Cheng, Y., Yang, S., Shao, M.. Direct observations indicate photodegradable oxygenated volatile organic compounds (OVOCs) as larger contributors to radicals and ozone production in the atmosphere. Atmospheric Chemistry and Physics, 22(6), 4117-4128. https://doi.org/10.5194/acp-22-4117-2022, 2022.

Wang T, Xue L, Brimblecombe P, Lam YF, Li L, Zhang L. Ozone pollution in China: A review of concentrations, meteorological influences, chemical precursors, and effects. Sci Total Environ. 575:1582-1596. https://doi.org/10.1016/j.scitotenv.2016.10.081, 2017.

Wang, T., Xue, L., Feng, Z., Dai, J., Zhang, Y., Tan, Y. Ground-level ozone pollution in China: a synthesis of recent findings on influencing factors and impacts. Environmental Research Letters, 17(6), 063003. https://doi.org/10.1088/1748-9326/ac69fe, 2022.

1505   Wesely, M.L., Hicks, B.B., A review of the current status of knowledge in a dry deposition. Atmos. Environ., 34, 2261-2282, https://doi.org/10.1016/S1352-2310(99)00467-7, 2000.

Xia, R., Luo, Y., Zhang, D. L., Li, M., Bao, X., Sun, J., On the diurnal cycle of heavy rainfall over the Sichuan Basin during 10–18 August 2020., Advances in Atmospheric Sciences, 38, 2183-2200,
1510   https://doi.org/10.1007/, 2021.

Xu, X., Ge, B., Lin, W. Progresses in the research of ozone production efficiency (OPE)., Adv. in Earth Science, 24(8), 845-853, https://doi.org/10.11867/j.issn.1001-8166.2009.08.0845, 2009.

Xue, L., Gu, R., Wang, T., Wang, X., Saunders, S., Blake, D., Louie, P. K. K., Luk, C. W. Y.,
1515   Simpson, I., Xu, Z., Wang, Z., Gao, Y., Lee, S., Mellouki, A., and Wang, W.: Oxidative capacity and radical chemistry in the polluted atmosphere of Hong Kong and Pearl River Delta region: analysis of a severe photochemical smog episode, Atmos. Chem. Phys., 16, 9891–9903, https://doi.org/10.5194/acp-16-9891-2016, 2016.

Yang L. H., D. J. Jacob, N. K. Colombia., Tropospheric NO_2 vertical profiles over South Korea
1520   and their relation to oxidant chemistry: Implications for geostationary satellite retrievals and the observation of NO_2 diurnal variation from space, https://doi.org/10.5194/egusphere-2022-1309, 2022.

Yang, X., Lu, K., Ma, X., Liu, Y., Wang, H., Hu, R., Zhang, Y. Observations and modeling of OH and HO2 radicals in Chengdu, China in summer 2019. Science of The Total Environment, 772,
1525   144829.https://doi.org/10.1016/j.scitotenv.2020.144829, 2021.

Yang, X., Lu, K., Ma, X., Gao, Y., Tan, Z., Wang, H., ... & Zhang, Y. Radical chemistry in the Pearl River Delta: observations and modeling of OH and HO 2 radicals in Shenzhen in 2018. Atmos. Chem. Phys., 22(18), 12525-12542. https://doi.org/10.5194/acp-22-12525-2022, 2022.
1530

Yu, C., Wang, Z., Xia, M., Fu, X., Wang, W., Tham, Y. J., Chen, T., Zheng, P., Li, H., Shan, Y., Wang, X., Xue, L., Zhou, Y., Yue, D., Ou, Y., Gao, J., Lu, K., Brown, S. S., Zhang, Y., and Wang, T.: Heterogeneous N_2O_5 reactions on atmospheric aerosols at four Chinese sites: improving the model representation of uptake parameters, Atmos. Chem. Phys., 20, 4367–4378,
1535   https://doi.org/10.5194/acp-20-4367-2020, 2020.

Yu, D., Tan, Z., Lu, K., Ma, X., Li, X., Chen, S., Zhang, Y. An explicit study of local ozone budget and NOx-VOCs sensitivity in Shenzhen China. Atmospheric Environment, 224, 117304. https://doi.org/10.1016/j.atmosenv.2020.117304, 2020.
1540

Zaveri, R. A., Easter, R. C., Fast, J. D., and Peters, L. K., Model for Simulating Aerosol Interactions and Chemistry (MOSAIC), J. Geophys. Res., 113, D13204, https://doi.org/10.1029/2007JD008782, 2008.

1545   Zhang, Q., Streets, D. G., Carmichael, G. R., He, K. B., Huo, H., Kannari, A., Klimont, Z., Park, I. S., Reddy, S., Fu, J. S., Chen, D., Duan, L., Lei, Y., Wang, L. T., and Yao, Z. L.: Asian emissions in 2006 for the NASA INTEX-B mission, Atmos. Chem. Phys., 9, 5131–5153, https://doi.org/10.5194/acp-9-5131-2009, 2009.

1550   Zhang, S., Sarwar, G., Xing, J., Chu, B., Xue, C., Sarav, A., Ding, D., Zheng, H., Mu, Y., Duan, F., Ma, T., and He, H.: Improving the representation of HONO chemistry in CMAQ and examining its impact on haze over China, Atmos. Chem. Phys., 21, 15809–15826, https://doi.org/10.5194/acp-21-15809-2021, 2021.

1555   Zhang, Y., Dai, J., Li, Q., Chen, T., Mu, J., Brasseur, G., Xue, L. Biogenic volatile organic compounds enhance ozone production and complicate control efforts: Insights from long-term observations in Hong Kong. Atmospheric Environment, 119917, https://doi.org/10.1016/j.atmosenv.2023.119917, 2023.

1560   Zhang, Y., Wen, X. Y., Wang, K., Vijayaraghavan, K., Jacobson, M. Z.,. Probing into regional O_3 and particulate matter pollution in the United States: 2. An examination of formation mechanisms through a process analysis technique and sensitivity study. Journal of Geophysical Research, 114. https://doi.org/10.1029/2009jd011900, 2009.

1565   Zheng, B., Tong, D., Li, M., Liu, F., Hong, C., Geng, G., Li, H., Li, X., Peng, L., Qi, J., Yan, L., Zhang, Y., Zhao, H., Zheng, Y., He, K., and Zhang, Q.: Trends in China's anthropogenic emissions since 2010 as the consequence of clean air actions, Atmos. Chem. Phys., 18, 14095–14111, https://doi.org/10.5194/acp-18-14095-2018, 2018

1570   Zhu, J. S. Wang, H. Wang, S. Jing, S. Lou, A. Saiz-Lopez, and B. Zhou, Observationally constrained modeling of atmospheric oxidation capacity and photochemical reactivity in Shanghai, China, Atmos. Chem. Phys., 20, 1217-1232, https://doi.org/10.5194/acp-20-1217-2020, 2020.

1575

1580

Table 1. Simplified chemical mechanisms used for the interpretation of model results

Num.	Reactions	Reaction rate constant (k)
Photolysis reactions		
R1	$O_3 + hv \rightarrow O(^1D) + O_2$	$j_{O(1D)}$ [a]
R2	$NO_2 + hv \rightarrow NO + O$	j_{NO2} [a]
R3	$HCHO + hv + O_2 \rightarrow 2\ HO_2 + CO$	j_{HCHO} [a]
R4	$OVOC_i + hv \rightarrow RO_{x,i}$	j_{OVOCi} [a,b]
R5	$HONO + hv \rightarrow NO + OH$	j_{HONO} [a]
Thermal reactions		
R6	$O(^1D) + M \rightarrow O(^3P) + M$	$3.20 \times 10^{-11} \times \exp(70/T)$
R7	$O + O_2 + M \rightarrow O_3 + M$	$6.00 \times 10^{-34} \times \exp(300/T)^{2.4}$
R8	$O(^1D) + H_2O \rightarrow 2\ OH$	2.20×10^{-10}
R9	$CH_4 + OH + O_2 \rightarrow RO_2\ (= CH_3O_2) + H_2O$	$2.45 \times 10^{-12} \times \exp(-1775/T)$
R10	$HC_i + OH + O_2 \rightarrow \alpha HO_2 + \beta RO_{2,i} +$ oxidation products	9.00×10^{-12} [b]
R11	$Alk_i + O_3 \rightarrow OH, HO_2, RO_{2,i}$	$1.20 \times 10^{-14} \times \exp(-2630/T)$ [b]
R12	$CO + OH + O_2 \rightarrow CO_2 + HO_2$	$1.50 \times 10^{-13} \times (1 + 6 \times 10^{-7} \times P)$
R13	$OH + O_3 \rightarrow HO_2 + O_2$	$1.70 \times 10^{-12} \times \exp(-940/T)$
R14	$HO_2 + O_3 \rightarrow OH + 2\ O_2$	$1.00 \times 10^{-14} \times \exp(-490/T)$
R15	$OH + HO_2 \rightarrow H_2O + O_2$	$4.80 \times 10^{-11} \times \exp(250/T)$
R16	$HO_2 + HO_2 + M \rightarrow H_2O_2 + O_2 + M$	$k0 = 6.90 \times 10^{-31} \times (300/T)^{1.00}$; $k1 = 2.60 \times 10^{-11}$; $f = 0.60$
R17	$HO_2 + RO_{2,i} \rightarrow ROOH_i + O_2$	$4.10 \times 10^{-13} \times \exp(750/T)$ [b]

R18	$RO_{2,i} + RO_{2,j} \rightarrow$ products	$5.00 \times 10^{-13} \times \exp(-424/T)$ [b] $1.90 \times 10^{-14} \times \exp(706/T)$ [b]
R19	$NO + O_3 \rightarrow NO_2 + O_2$	$3.00 \times 10^{-12} \times \exp(-1500/T)$
R20	$NO + HO_2 \rightarrow NO_2 + OH$	$3.50 \times 10^{-12} \times \exp(250/T)$
R21	$NO + RO_{2,i} + O_2 \rightarrow$ carbonyl $+ NO_2 + HO_2$	$2.80 \times 10^{-12} \times \exp(300/T)$ [b]
R22	$NO + RO_{2,i} \rightarrow RONO_{2,i}$	$4.20 \times 10^{-12} \times \exp(-150/T)$ [c]
R23	$NO_2 + OH + M \rightarrow HNO_3 + M$	$k0 = 2.00 \times 10^{-30} \times (300/T)^{3.0}$; $k1 = 2.50 \times 10^{-11}$; $f = 0.60$ [d]
R24	$NO + OH \rightarrow HONO$	$k0 = 7.00 \times 10^{-31} \times (300/T)^{-2.6}$; $k1 = 3.60 \times 10^{-11}$; $f = -0.1$ [d, e]
R25	$NO + NO_2 + H_2O \rightarrow 2\ HONO$	5.00×10^{-40} [e]
R26	$HONO + HONO \rightarrow NO + NO_2 + H_2O$	1.00×10^{-20} [e]
R27	$HONO + OH \rightarrow NO_2 + H_2O$	2.50×10^{-12} [e]
Heterogeneous reactions		
R28	$HO_2 \rightarrow H_2O$	$\gamma = 0.1$ [f, g]
R29	$N_2O_5 \rightarrow 2\ HNO_3$	Bertram and Thornton (2009) [f]
R30	$NO_3 \rightarrow HNO_3$	$\gamma = 1.00 \times 10^{-3}$ [f, h]
R31	$NO_2 \rightarrow 0.5\ HONO + 0.5\ HNO_3$	Zhang et al. (2021) [f]

Notes.

k is a rate constant. First-order rate constants are given per second (s^{-1}); second-order rate constants are in units of cm^3 molecule^{-1} s^{-1}; and third-order constants are in units of cm^6 molec.$^{-2}$ s^{-1}. [M] is the total air concentration (molecules cm^{-3}); T is the air temperature (K);

[a] photolysis of O(^{1}D), NO2, HCHO, OVOCs and HONO. Each reaction rate is taken from MOZART-4 (Emmons et al., 2010).

[b] Specific kinetics data for each compound are taken from MOZART-4 (Emmons et al., 2010). Here, the HC, Alk., RO2, ROOH refer to C2H4, C2H4, CH3O2, CH3OOH, respectively.

[c] RO2 and RO2NO2 refer to ALKO2 (lumped alkane peroxy radical) and ONIT (organic nitrate).

[d] Refer to TROE function in WRF-Chem v 4.1.2 (Skamarock et al., 2019)

1595 [e] Zhang et al. (2021).
      [f] Calculation of reaction rate refer to Equation (5)
      [e] Gaubert et al. (2020).
      [h] Liu and Wang. (2020).

1600

1605 **Table 2.** Location of the observational sites or areas referred to in the present study

Site name	Latitude	Longitude	Site type
Beijing	39.90° N-40.10° N	116.30° E-116.50° E	Urban sites
Shanghai	31.10° N-31.30° N	121.40° E-121.60° E	Urban sites
Guangzhou	23.00° N-23.20° N	113.10° E-113.30° E	Urban sites
Chengdu	30.50° N-30.70° N	103.90° E-104.10° E	Urban sites
Wangdu	38.66° N	115.25° E	Rural site
Heshan	22.73°N	112.93°E	Rural site
Waliguan	36.17° N	100.54° E	Mountainous/Background site
Hok Tsui	22.22° N	114.25° E	Coastal/Background site

1610

1615

Table 3. Sensitivity experiments

Modeling cases	Description
Het-All	With all heterogeneous reactions and all other HONO sources
No-HetHO2-Aero	Without HO_2 uptake on aerosols
No-HetNO3-Aero	Without NO_3 uptake on aerosols
No-HetN2O5-Aero	Without N_2O_5 uptake on aerosols
No-HetNO2-Aero	Without NO_2 uptake on aerosols
No-Het-Aero	Without HO_2, NO_3, N_2O_5, and NO_2 uptake reactions on aerosols
No-Phot	Without aerosol effects on light extinction and photodissociation
No-Het-Aero-Phot	Without HO_2, NO_3, N_2O_5, and NO_2 uptake reactions on aerosols and aerosol effects on light extinction and photodissociation
No-HONO	Without HONO sources
No-Het-HONO-Phot	Without HO_2, NO_3, N_2O_5, and NO_2 uptake reactions on aerosols, other HONO sources and aerosol effects on light extinction and photodissociation

1620

1625

Table 4. Comparison between values of the production rate of RO_x [Units: ppbv h^{-1}] derived from local observations and calculated by our regional model in July 2018.

1630

Location	Period	Me.[a]	Ca.[b]	Me.[a]	Ca.[b]	Me.[a]	Ca.[b]	Me.[a]	Ca.[b]
		Peak value[c]		HONO[d]		HCHO[e]		Ozone[f]	
Beijing[g]	Spring 2018	7.0	7.5	4.0	4.0	1.5	2.0	1.5	1.5
Shanghai[h]	Summer 2021	4.5	5.0	2.5	1.0	1.0	1.0	1.0	1.5
Guangzhou[i]	Autumn 2018	5.6	6.0	2.0	3.0	1.5	1.0	1.0	1.5
Chengdu[j]	Summer 2019	7.0	7.5	2.0	2.5	2.0	1.5	1.5	2.0
Wangdu[k]	Summer 2014	5.0	4.8	2.0	2.0	1.0	2.0	1.5	1.0
Heshan[l]	Autumn 2014	4.0	1.1	2.0	0.5	1.5	0.4	0.5	0.5

[a] Measured value in relevant periods; [b] Calculated value in our study in July 2018; [c] Peak value of production rate of RO_x; [d, e, f] Peak value of the production rate of RO_x from the photolysis of [d]

1635   HONO, [e] HCHO and [f] O_3; [g, h, i, j, k, l] Observations from the studies of [g] Whalley et al. (2021), [h] Zhu et al. (2021), [i] Wang et al. (2022), [j] Yang et al., (2022), [k] Tan et al., (2017) and, [l] Tan et al. (2019).
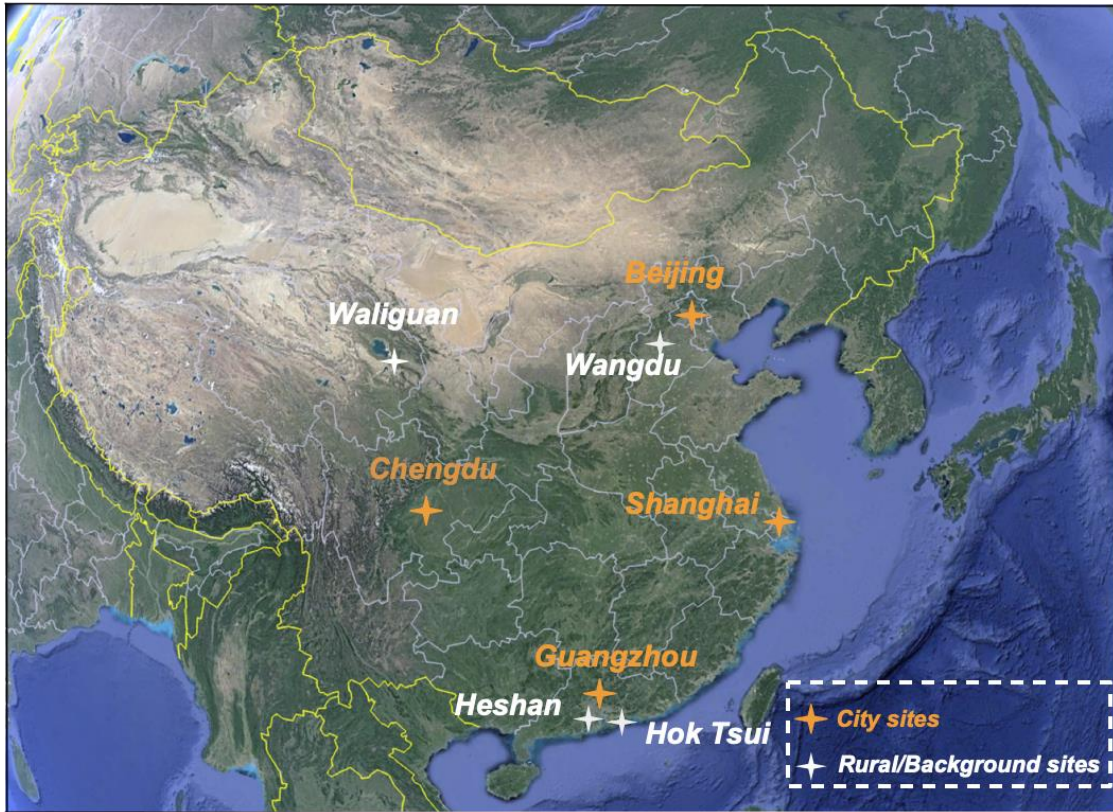
Figure 1. Location of sites (stars) considered in our analysis (from Google Maps).
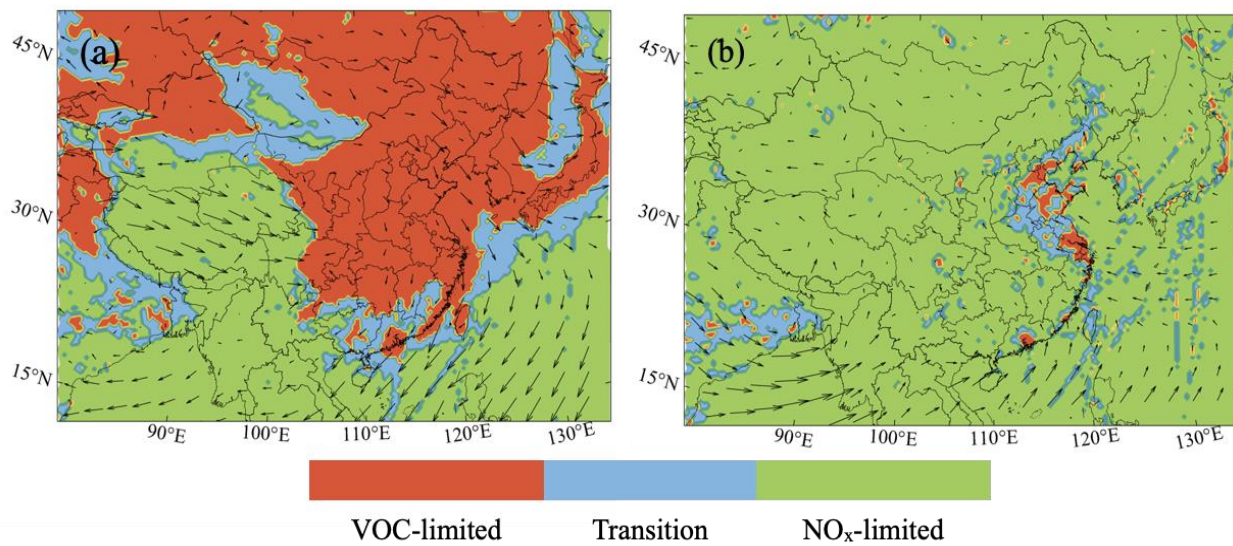
Figure 2. Display of regions in which the ozone production is limited by the availability of nitrogen oxides (NO$_X$-limited, in green), and volatile organic carbon (VOC-limited, in red) in January (a) and July (b), 2018. The regions with intermediate conditions (Transition) are shown in blue. The indicator used to define these regions is the production rate ratio between Hydrogen peroxide (H$_2$O$_2$) and Nitric acid (HNO$_3$) [P(H$_2$O$_2$)/P(HNO$_3$)].
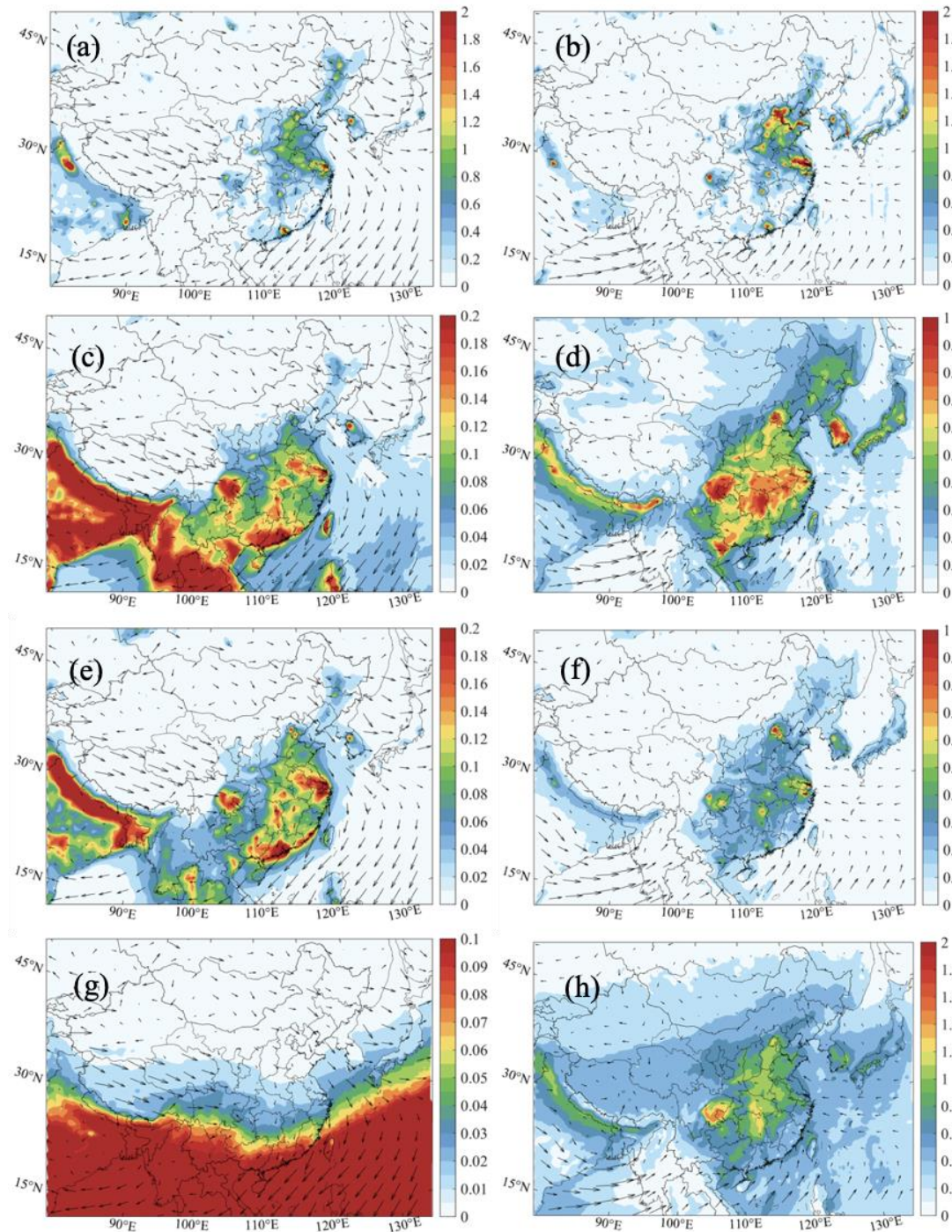
Figure 3. Spatial distribution of the production rate of RO_x (RO_2+HO_2+OH) [$P(RO_x)$, Unit: ppbv h^{-1}] (*Het-All* case) from the photolysis of nitrous acid (HONO) (a, b), formaldehyde (HCHO) (c, d), non-HCHO oxidized volatile organic compounds (OVOCs) (g, h) and O_3 (Reactions between O^1D and H_2O; e, f) in the daytime (08:00-19:00 Local Standard Time (LST)) of January (left column: a, c, e, g) and July (right column: b, d, f, h). Note the difference in scales among panels.

49
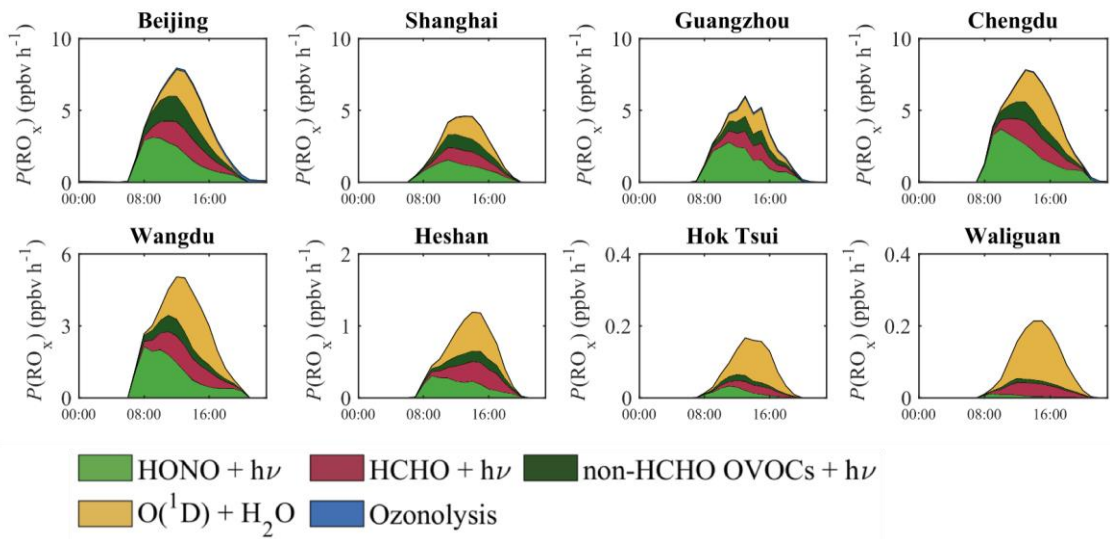
1670

Figure 4. Diurnal variation of the production rate of RO_x [$P(RO_x)$, Unit: ppbv h^{-1}] in different regions of China calculated for July 2018.
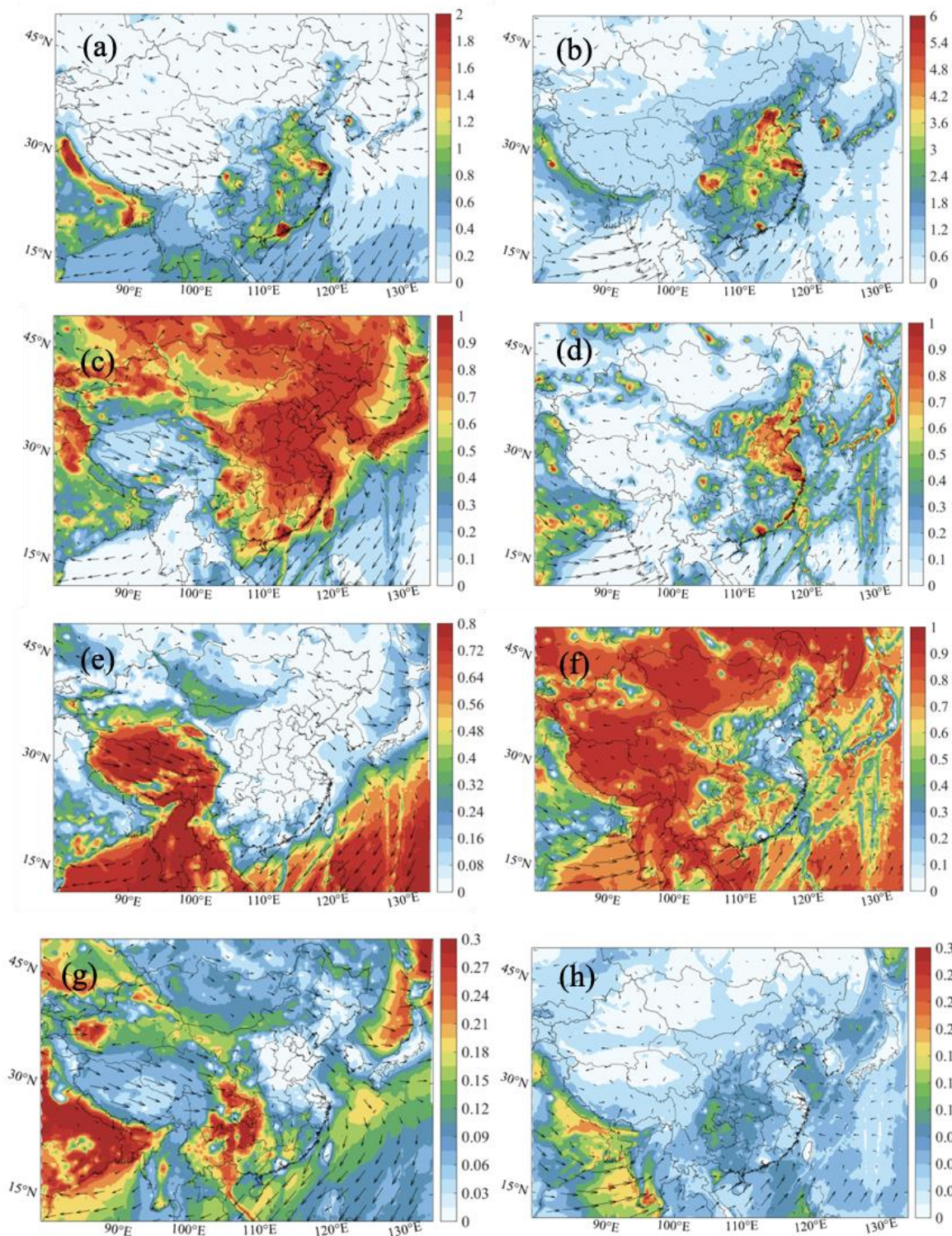
1675 **Figure 5**. Spatial distribution of destruction rate of RO_x [$D(RO_x)$, Unit: ppbv h^{-1}] (a, b) and the relative contribution $L_N/D(RO_x)$ (c, d), $L_H/D(RO_x)$ (e, f) and $L_{het}/D(RO_x)$ (g, h) in the daytime of January (left column: a, c, e, g) and July (right column: b, d, f, h).
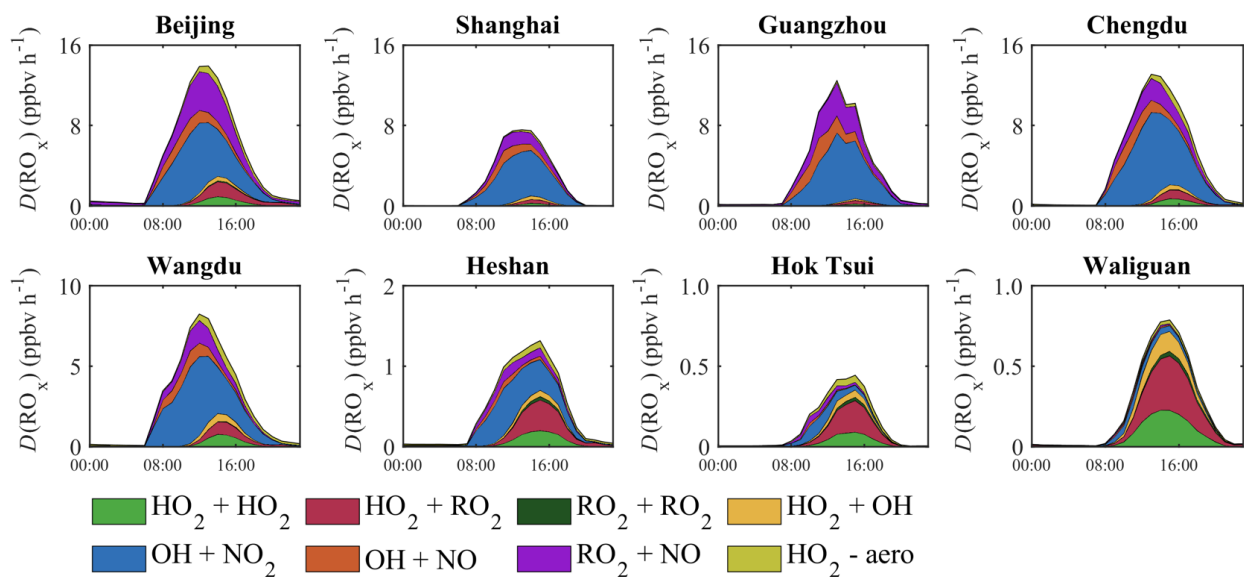
Figure 6. Diurnal variation of the photochemical destruction rate of RO_x [$D(RO_x)$, Unit: ppbv h^{-1}] in eight sites of China for July 2018. The contributions to the destruction rate are the following: L_H accounts for the following reactions: $HO_2 + HO_2$, $HO_2 + RO_2$, $RO_2 + RO_2$, and $OH + HO_2$. L_N accounts for $OH + NO_2$ and $RO_2 + NO$. L_{HO2} to the uptake of HO_2 by particles.
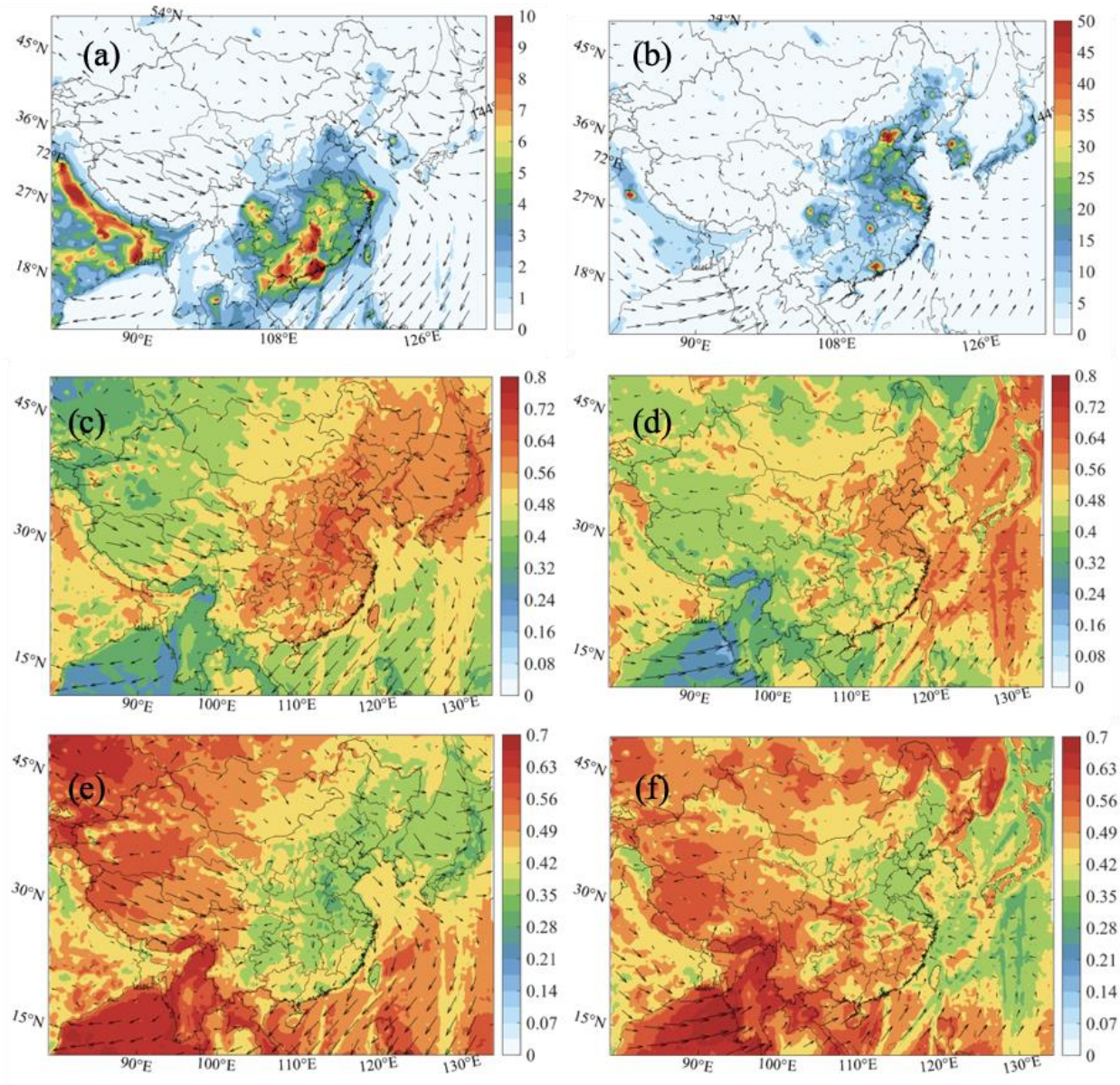
Figure 7. Spatial distribution of production rate of odd oxygen [$P(O_x)$, Unit: ppbv h^{-1}] (a, b) and the relative contributions from the reactions between HO$_2$ and NO (c, d) and RO$_2$ and NO (e, f) in the daytime of January (left column: a, c, e) and July (right column: b, d, f).
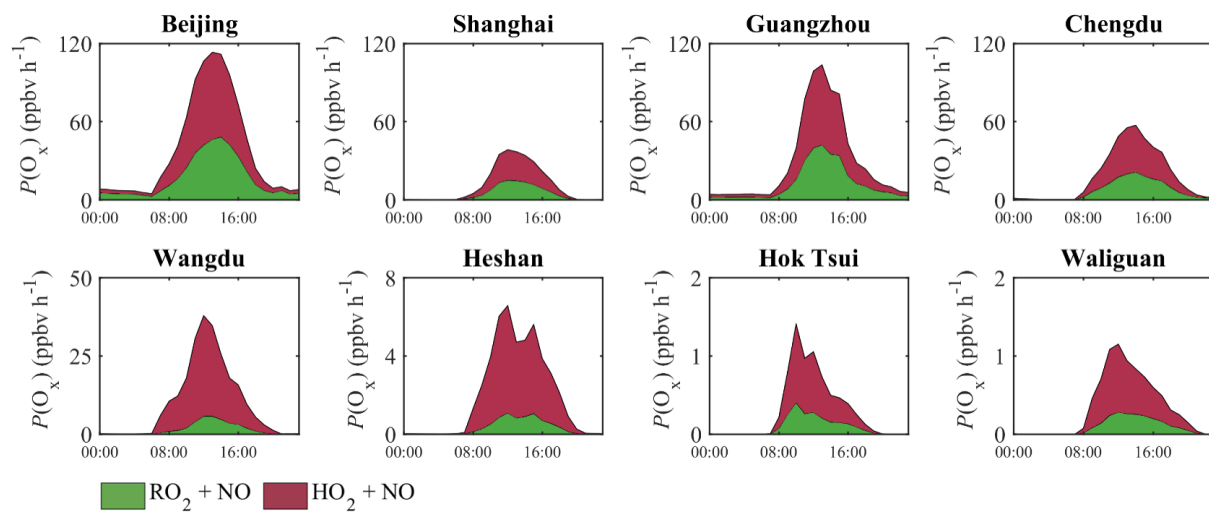
Figure 8. Diurnal variation of the O_x production rate [$P(O_x)$, Unit: ppbv h^{-1}] in different regions of China for July 2018.
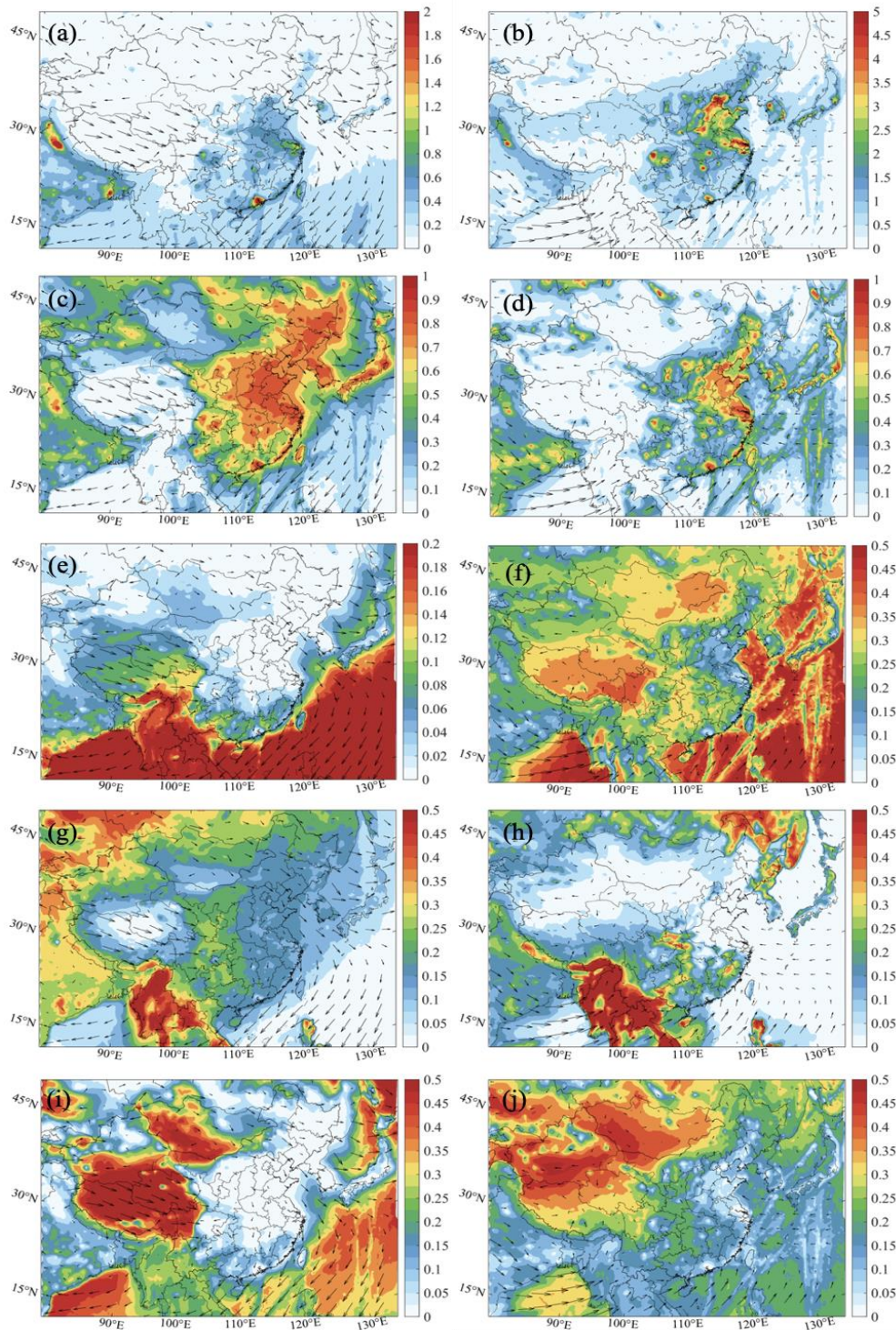
Figure 9. Spatial distribution of destruction rate of odd oxygen (a, b) [$D(O_x)$, Unit: ppbv h^{-1}] (*Het-All* case) and the relative contributions from the reactions of OH with NO_2 (c, d), $O(^1D)$ with H_2O (e, f), Alkene with O_3 (g, h) and HO_2 with O_3 (i, j) in the daytime of January (left column: a, c, e, g, i) and July (right column: b, d, f, h, j).
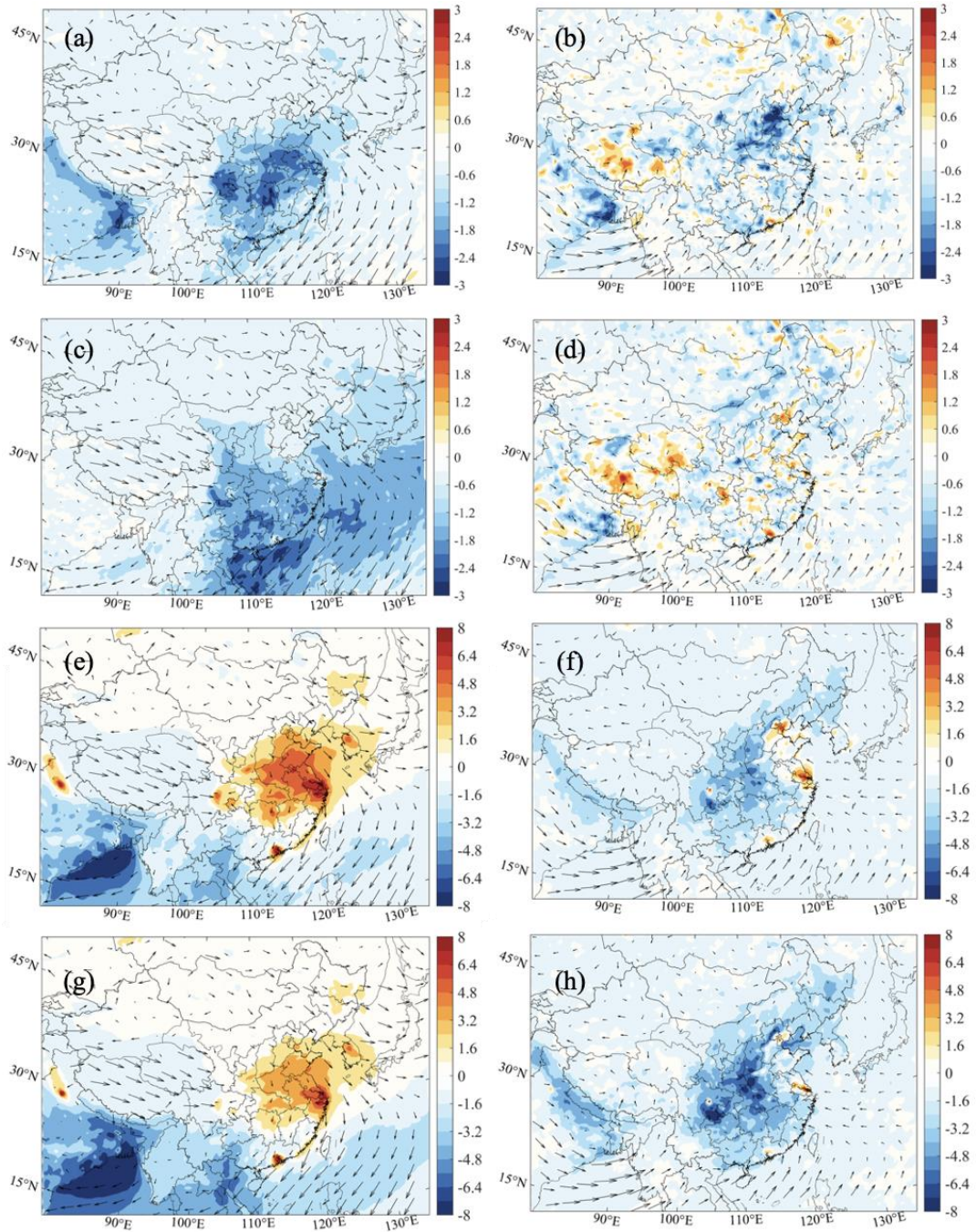
Figure 10. Spatial distribution of the response of the monthly average surface O_3 concentration [Unit: ppbv] to the aerosol uptake by HO_2 (a, b; *Het-All* minus *No-HetHO2-Aero*), N_2O_5 (c, d, *Het-All* minus *No-HetN2O5-Aero*), NO_2 (e, f, *Het-All* minus *No-HetNO2-Aero*), and to the uptake by all these processes (g, h, *Het-All* minus *No-Het-Aero*). The results are shown for the daytime of January (left column: a, c, e, g) and July (right column: b, d, f, h) of 2018.
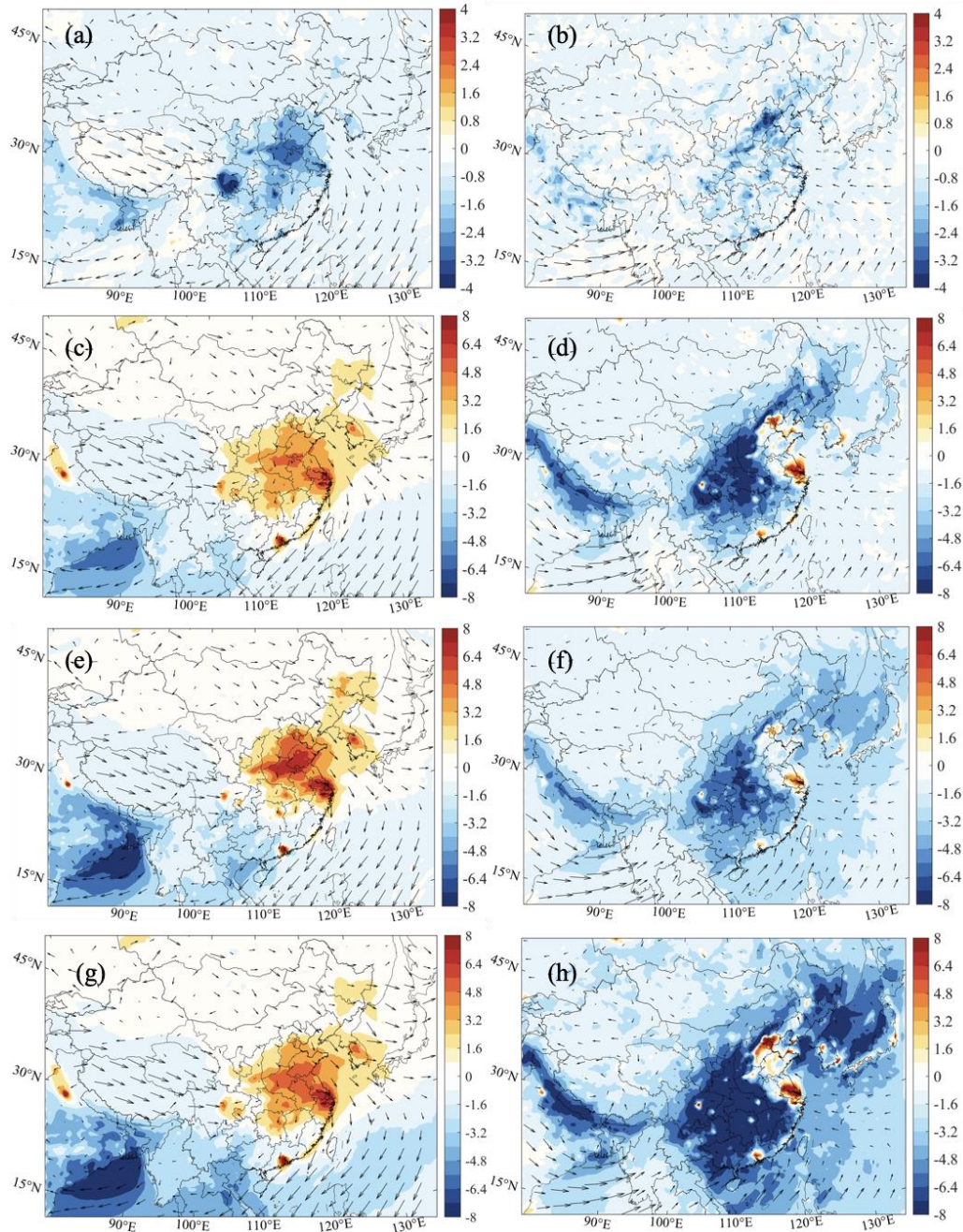
Figure 11. Changes in the surface concentrations of daytime O_3 [Unit: ppbv] resulting from the effect of aerosol-related solar light extinction on photolysis for January (a) and July(b) (*Het-All* minus *No-Phot*), the combined effect of photolysis and aerosol uptake for January (c) and July (d) (*Het-All* relative to *No-Het-Aero-Phot*), effects of NO_2 uptake by aerosols and on the surfaces as well as direct HONO emissions from traffic and gas phase formation for January (e) and July (f) (*Het-All* minus *No-HONO*), and from all NO_2, N_2O_5, NO_3 and HO_2 uptake processes photolysis effects and other HONO sources for January (g) and July (h) (*Het-All* minus *No-Het-HONO-Phot*).

1725
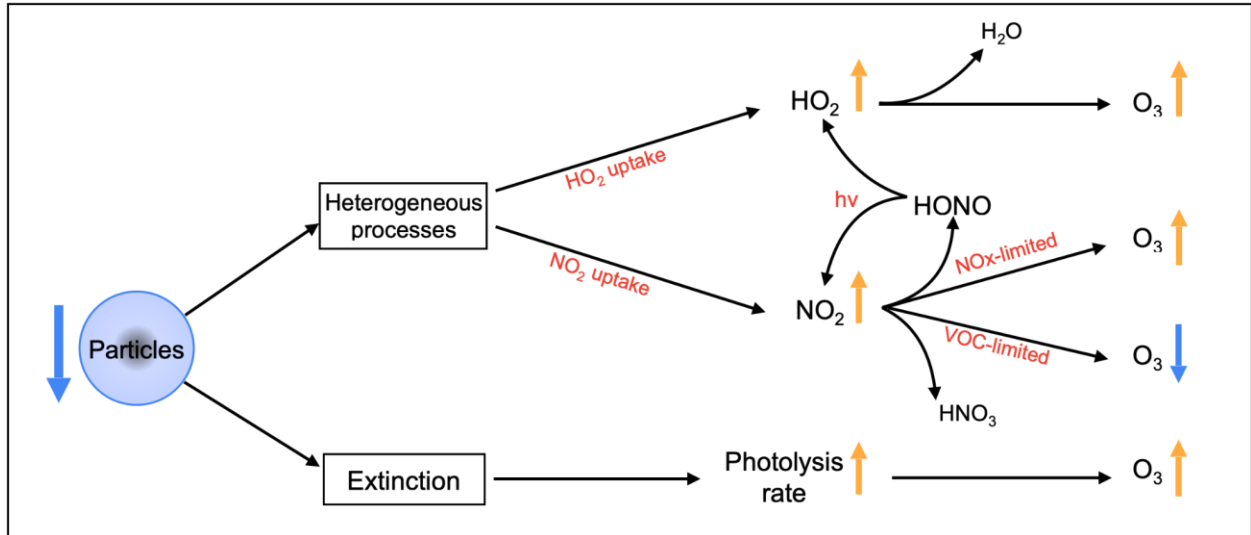
Figure 12. Schematic for the impact of aerosol through aerosol extinction of solar radiation and
1730   heterogeneous processes on ozone concentration. Arrows represent the changes in chemicals and
photolysis rate associated with the reduction of aerosols.
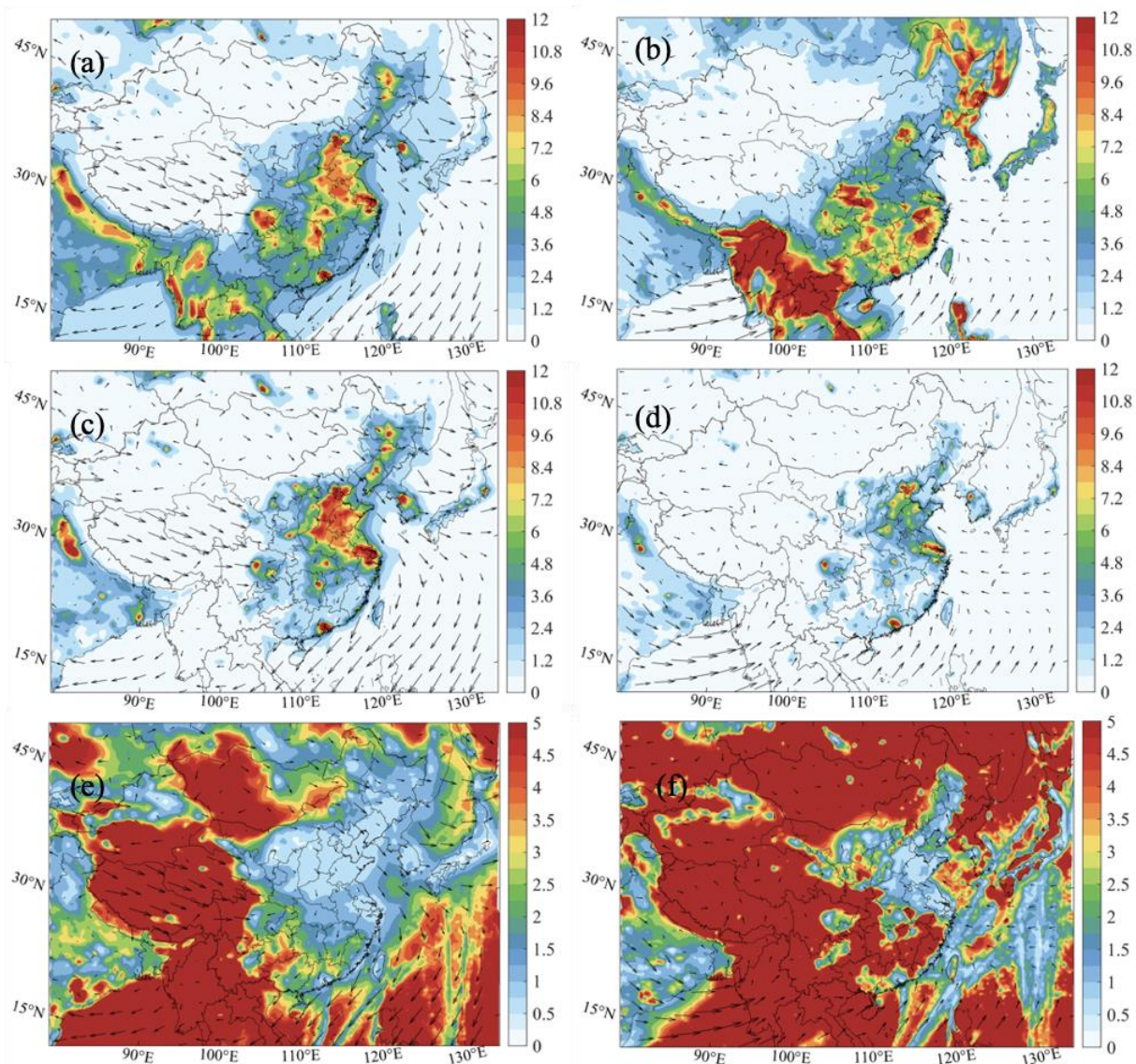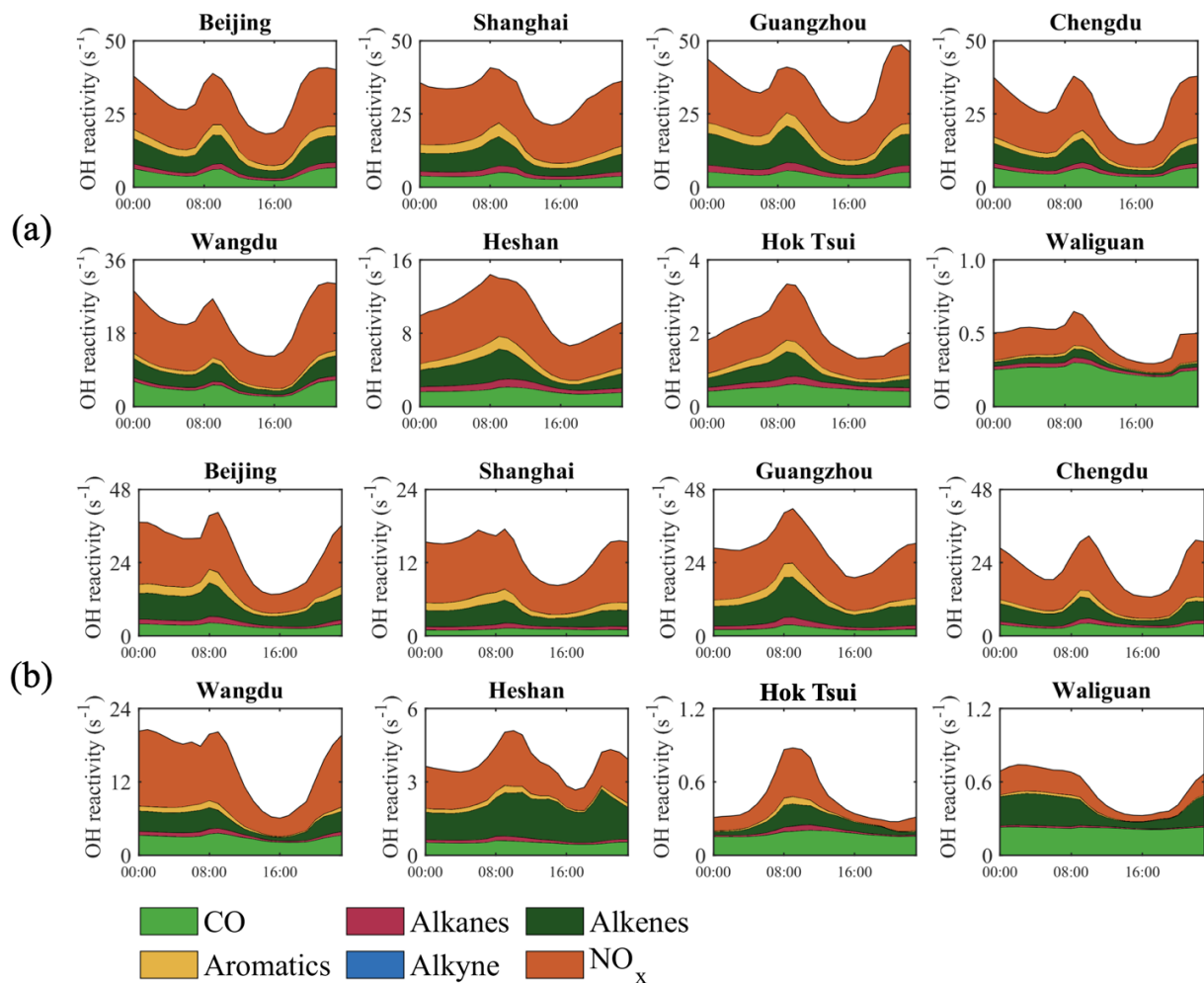
1735

1740

1745

Figure 13. Spatial distribution of reactivity of VOCs (VOC^R) [Unit: s^{-1}] and NO$_x$ ($NO_x{}^R$; c, d) [Unit: s^{-1}], VOC^R to $NO_x{}^R$ ratio (e, f) (*Het-All* case) for daytime conditions in January (left column: a, c, e) and July (right column: b, d, f).

Figure 14. Diurnal variation of different contributions to the OH reactivity [Unit: s⁻¹] in cities and remote sites. The values associated with alkenes include the contribution of biogenic isoprene and terpenes. The two upper rows refer to January (a) and the two lower rows to July (b).
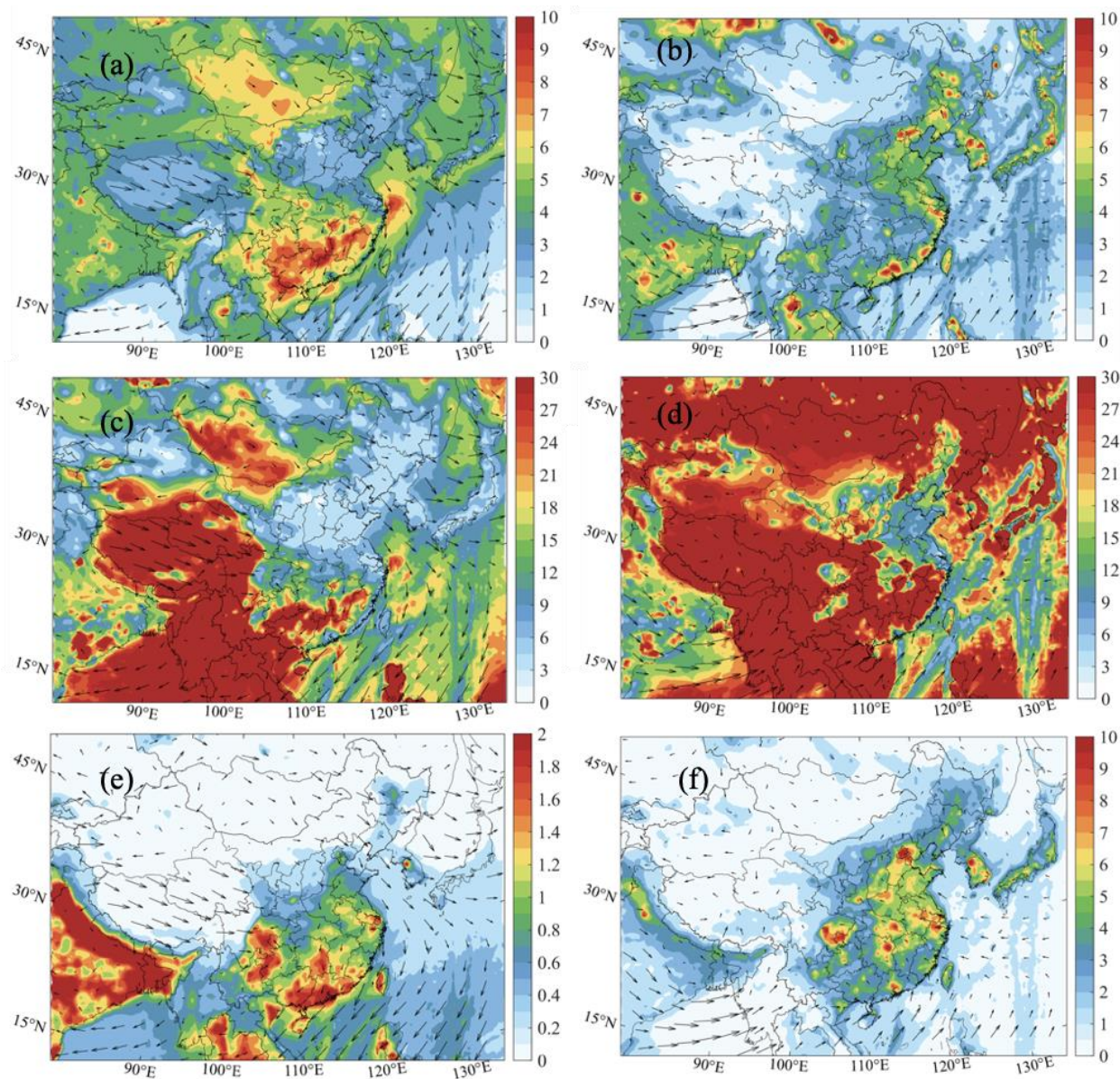
Figure 15. Spatial distribution of radical chain length (*ChL*) in January (a) and July(b), ozone production efficiency (*OPE*) in January (c) and July(d), and atmospheric oxidation capacity (*AOC* [Unit: 10^7 molecular cm^{-3} s^{-1}]) in January (e) and July(f) for daytime conditions extracted from the *Het-All* case.
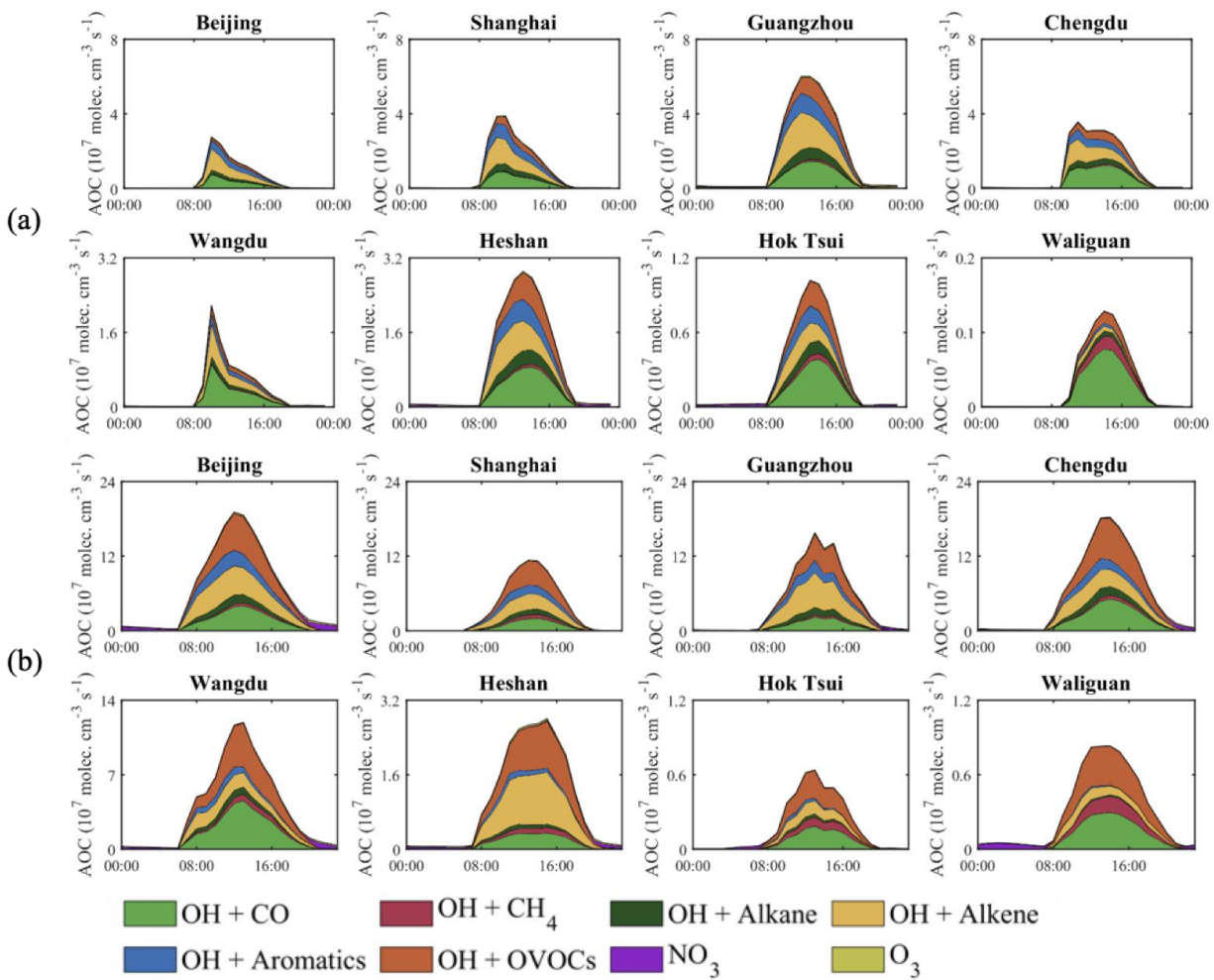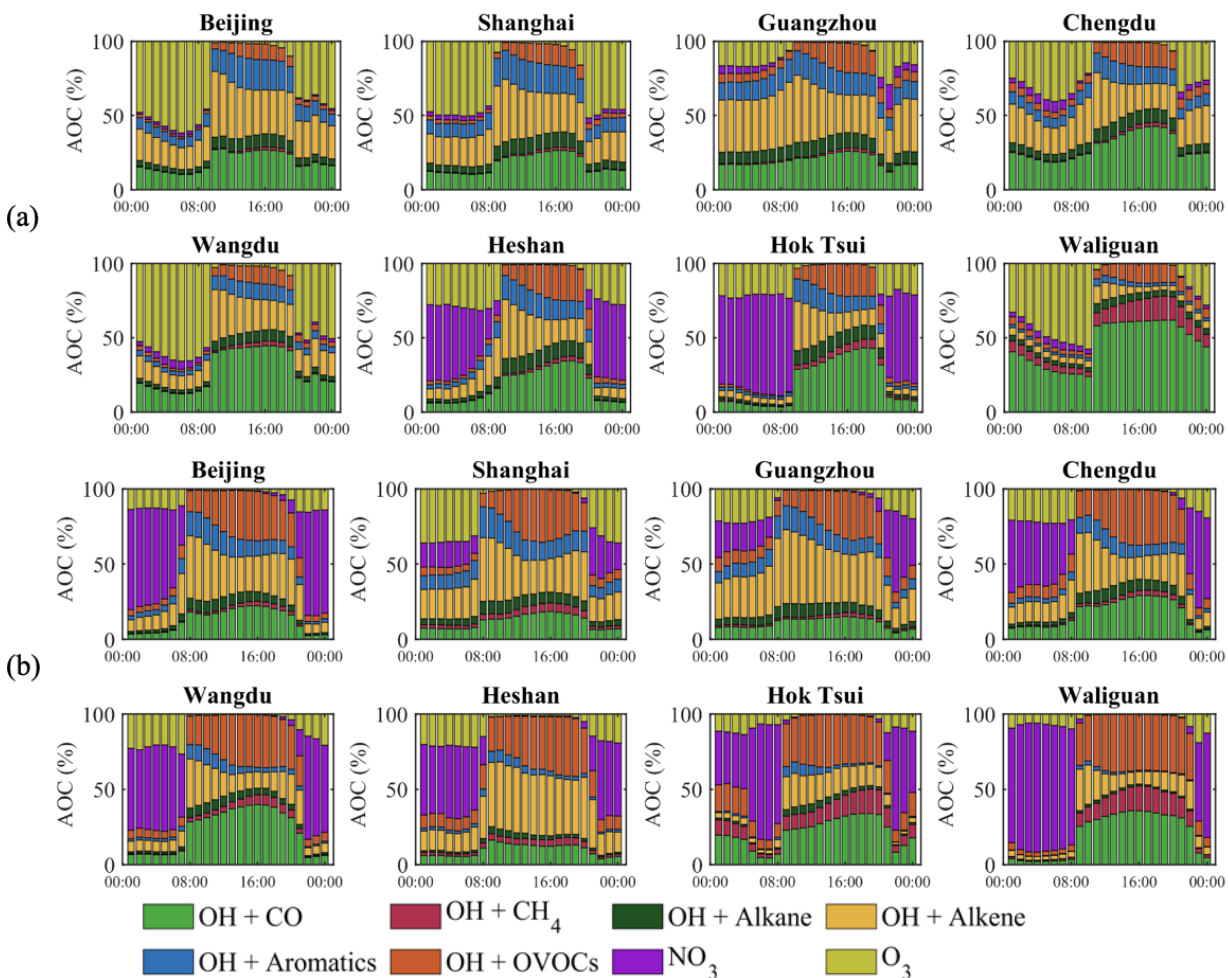
Figure 16. Diurnal variation of the atmospheric oxidizing capacity (*AOC*) [Unit: 10^7 molecules cm^{-3} s^{-1}] in cities and remote sites. The effect of alkenes includes the contribution of biogenic isoprene and terpenes, while the effect of OVOCs includes the contribution of formaldehyde. The two upper rows refer to January (a) and the two lower rows to July (b).

Figure 17. Same as Fig. 16, but expressed in relative terms [Unit: %] and highlighting the nighttime contribution to the *AOC* value. The two upper rows refer to January (a) and the two lower rows to July (b).